

Rational Design of Hydrogen Evolution Reaction Electrocatalysts for Commercial Alkaline Water Electrolysis

Hao Guan Xu, Xin Yu Zhang, Yeliang Ding, Huai Qin Fu, Rui Wang, Fangxin Mao, Peng Fei Liu,* and Hua Gui Yang*

With the further exploitation of renewable energy sources, electrochemical hydrogen evolution reaction (HER) is considered a key technology to solve environmental problems and achieve global carbon neutrality. Currently, alkaline water electrolyzers (AWEs) have been revitalized as a traditional electrolytic water production industry, yet they face great challenges in achieving new technological breakthroughs due to the catalytic properties of electrode materials. In alkaline media, besides the slow kinetics of oxygen evolution reaction, the sluggish HER needing water dissociation and the mass transfer problems at high current densities are among the major factors limiting the development of alkaline water electrolysis for industrial applications. Therefore, it is of great importance to design HER electrocatalysts with high activity and stability at high current densities ($>500 \text{ mA cm}^{-2}$) for industrial applications at the “Research and Development level” (R&D level). Herein, a brief overview of the development of AWEs at the industrial scale is presented, and some mainstream recognized catalysis mechanisms for HER in alkaline electrolytes are summarized. Based on the requirements of industrial application and theoretical guidance, the activation strategies of HER electrocatalysts are also summarized. This review will propose new insights into the future development of alkaline water electrolysis.

1. Introduction

Since rapid urbanization and modernization propelled human society to unprecedented heights, excessive consumption of traditional fossil fuel energy has triggered severe environmental pollution and energy crises,^[1,2] necessitating the urgent development of clean, renewable, and low-carbon technology to upgrade the existing energy structure.^[3] Hydrogen, with its competitive characteristics of high-quality energy density (about 120 MJ kg), zero pollution (burning to produce water), and broad applications (i.e., industrial usage and transportation), shows great promise for a safe, clean, and sustainable energy future away from the carbon cycle. Currently, the main technologies for hydrogen production consist of the thermochemical reforming of traditional energy sources and biomass, water electrolysis, and photocatalysis. Among these, water electrolysis through renewable energy sources stands out as it enables the decarbonized production of hydrogen with high purity and facilitates the supply balance between

hydrogen and the grid that is driven by renewable energy. In addition, with the utilization of renewable energy, electrocatalytic water splitting is becoming increasingly competitive in terms of cost, showing great potential to complement and replace gray hydrogen in the future.^[4]

Since its discovery in 1789, hydrogen production from water electrolysis has been flourishing for more than 200 years. The International Energy Agency has reported that the process of instrument innovation for water electrolysis to produce hydrogen has made great progress in recent years. Globally, more than 500 MW of total installed capacity was commissioned in 2021, and the total installed capacity is expected to grow to more than 1 GW by the end of 2022.^[5] Currently, alkaline water electrolyzers (AWEs) and acid water electrolyzers, such as proton exchange membrane water electrolyzers (PEMWES), have a mature technology level in the market. As a rapidly developing industrial technology in recent years, PEMWES have been successfully marketed because of their many advantages, such as high purity of H₂ production, fast response time, low side reactions, and high current density. However, the high corrosiveness of the acidic environment has led to the use of scarce, expensive materials and components such as noble metal catalysts (such as Pt, Ir,

H. G. Xu, X. Y. Zhang, F. Mao, P. F. Liu, H. G. Yang
Key Laboratory for Ultrafine Materials of Ministry of Education
School of Materials Science and Engineering
East China University of Science and Technology
Shanghai 200237, China
E-mail: pfliu@ecust.edu.cn; hgyang@ecust.edu.cn

Y. Ding, R. Wang
China General Nuclear New Energy Holdings Co., Ltd.
Beijing 100071, China

H. Q. Fu
Centre for Catalysis and Clean Energy
Gold Coast Campus
Griffith University
Gold Coast, QLD 4222, Australia

 The ORCID identification number(s) for the author(s) of this article can be found under <https://doi.org/10.1002/sstr.202200404>.

© 2023 The Authors. Small Structures published by Wiley-VCH GmbH. This is an open access article under the terms of the Creative Commons Attribution License, which permits use, distribution and reproduction in any medium, provided the original work is properly cited.

DOI: [10.1002/sstr.202200404](https://doi.org/10.1002/sstr.202200404)

and Ru) and titanium-based collectors, which further increase the deployment cost of PEMWES. Compared with the PEMWES, the AWEs still dominate the hydrogen production market due to their mature equipment technology and low manufacturing and maintenance costs.^[4,6,7]

Although a mature industrial system has been set up, alkaline water electrolysis for hydrogen production still suffers from a high-cost gap compared to conventional hydrogen production methods. For example, the cost of hydrogen produced by methane reforming is in the range of \$0.90–1.75 kg_{H₂}⁻¹, while the cost of electrolytic hydrogen is often over \$3.00 kg_{H₂}⁻¹.^[7,8] In addition to coupling renewable energy with the electrolyzer to obtain cost-efficient electricity, developing effective, stable, and non-noble electrocatalysts is an effective approach to lowering electrolysis's energy requirement and extending the life of the device.

However, despite the rapid development of industrial electrolytic hydrogen production technology, there is an unsatisfactorily large gap in the matching academic research. For example, high alkaline concentrations are generally used as the electrolyte in commercial AWEs (\approx 30% KOH), while relatively low alkaline concentrations (0.1 or 1 M KOH) are applied in a laboratory setting. In addition, commercial electrolytic hydrogen production puts more attention on enhancing the stability of the electrocatalyst than on electrocatalytic performance. Unlike the nanomaterials used as catalysts in most academic studies, Raney nickel (nickel–aluminum alloys) can be operated at constant currents of 200–500 mA cm⁻² for tens of thousands of hours in extreme industrial environments, but it requires large overpotentials.^[9] This is far greater than the low operating current density of 10 mA cm⁻² as well as the tens of hours evaluation scale for those nanocatalysts with “excellent activity” in academic studies.^[10,11] **Table 1** summarizes the difference between industrial and laboratory-scale electrolytic water technologies. Water electrolysis consists of two half-reactions; the hydrogen evolution reaction (HER) on the cathode and the oxygen evolution reaction (OER) on the anode. Under alkaline conditions, the slow and complex four-electron transfer process of the OER has been fully emphasized in academia as well as industry, which has promoted the development of a large number of valid Ni-based catalysts.^[12,13]

Table 1. Comparison of alkaline HER catalyst on industrial and laboratory stage.

	Commercial alkaline water electrolyzers (AWEs)	Laboratory alkaline water splitting
Equipment	Flow-through diaphragm electrolyzer	H-type electrolyzer
Electrolyte	30 wt% KOH (\approx 6 M KOH)	1 (or 0.1) M KOH
Electrode materials	Nickel alloy (Raney nickel)	Nanometallic materials
Electrode area	>100 cm ²	1 cm ²
Operating temperature	60 °C–80 °C	25 °C
Operating pressure	2–10 bar	1 bar
Stability	10–20 years	Several hundred hours
Performance evaluation standards	Overpotential of electrode areas at 200–400 cm ²	Overpotential of electrode areas at 10–100 cm ²

In contrast, although HER seems to have a simpler activation mechanism requiring two-electron transfer steps, the lack of clarity in the HER mechanism under alkaline conditions often limits further exploitation of HER catalysts.^[14] Meanwhile, the limitation of mass transfer at high current densities and catalyst stability issues likewise affect the industrial application of laboratory-stage HER catalysts.^[15,16] Therefore, there is an urgent need to summarize the field of HER catalysts at high current densities. This review presents recent progress on HER electrocatalysts that may be suitable for industrial AWEs. Through an overview on the development of AWEs, the necessity of developing novel HER catalysts is clarified. We propose current challenges and design strategies in designing high-performance industrial HER electrocatalysts based on our understanding of the HER mechanism in alkaline media (**Figure 1**). Finally, the prospects and challenges of developing HER catalysts at the laboratory stage that are compatible with industrial applications are described, which provide new insights to explore new models for combining laboratorial and industrial investigations.

2. History of Alkaline Water Electrolysis Development and Recent Industrial Status

Alkaline water electrolysis has been developed for more than 200 years (**Figure 2**). In 1789, Troostwijk and Deiman first discovered the phenomenon of electrolysis of water, which kicks off the production of hydrogen via electrolysis.^[17] After that, Faraday's law of electrolysis was published to quantify electrical energy consumption and gas production, which formally supported hydrogen production by water electrolysis. In fact, the real industrialization of hydrogen production from water electrolysis was marked by the development of the Gramme machine in 1869 and the first unipolar water electrolysis plant in Lachinov in 1888.^[18] By the turn of the 20th century, more than 400 industrial electrolysis cells were in operation by the beginning of the 20th century.^[19] After that, alkaline electrolysis entered its first “blowout” period (1920–1970s). Many technological innovations in industrial water electrolysis occurred during this period, and they continue to occur today. For example, in terms of electrolyzer design, a bipolar configuration electrolyzer with a press filter effect was successfully developed to improve the efficiency of hydrogen production due to severe ohmic losses in monopolar electrolyzers. In addition, the discovery of Raney nickel and its official approval for use in alkaline electrolyzers around 1957 further reduced the hydrogen production overpotential and successfully lowered the operating temperature to 80 °C, which reached a new level in alkaline water electrolysis for hydrogen production and applications.^[20] The technological innovation led to the deployment of new projects. The first large 100 MW large-size electrolysis plant was launched in Canada for ammonia fertilizer production, and the development of highly modular units further simplified the installation and modulation process while promoting electrolytic hydrogen production efficiency.^[20] However, after the 1970s, the rise of the petrochemical industry led to the emergence of more competitive methane-reforming hydrogen production, resulting in a brief “stagnant period” for hydrogen production by water electrolysis. After the 1990s, the geopolitical energy crisis and the environmental problem caused by fossil

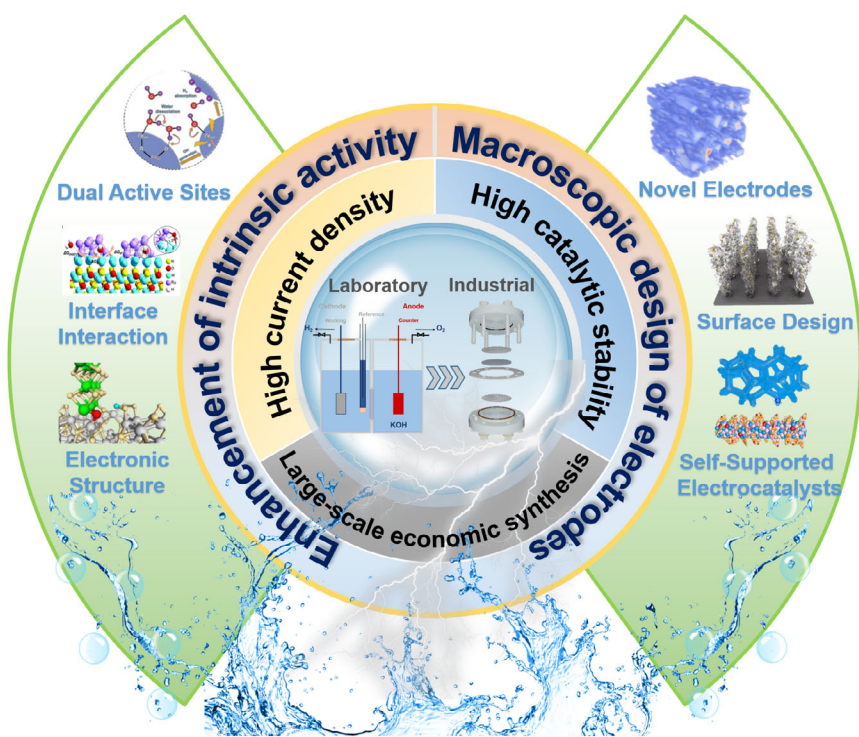


Figure 1. Summarized design strategies of hydrogen evolution reaction electrocatalysts for commercial alkaline water electrolysis, based on the enhancement of catalyst intrinsic activity and macroscopic electrode structure, respectively. Reproduced with permission.^[89] Copyright 2015, Springer Nature. Reproduced with permission.^[101] Copyright 2022, Elsevier. Reproduced with permission.^[117] Copyright 2019, Wiley-VCH GmbH. Reproduced with permission.^[150] Copyright 2020, Springer Nature. Reproduced with permission.^[168] Copyright 2022, Elsevier.

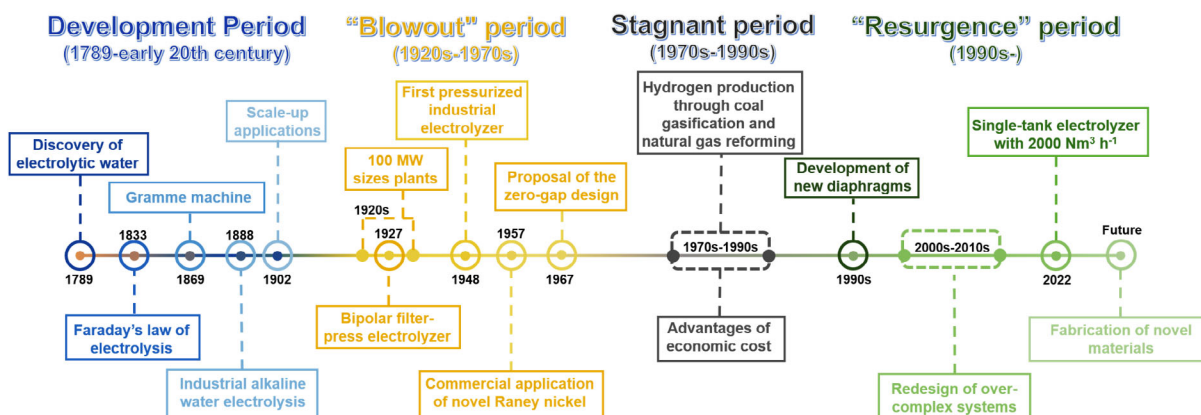


Figure 2. The development course of alkaline water electrolysis. Roughly, it can be divided into four different stages: the development period, the “blowout” period, the stagnation period, and the “resurgence” period.

fuel consumption revived the electrolytic hydrogen industry. For the traditional alkaline water electrolysis process, carcinogenic asbestos diaphragms were replaced by other materials (e.g., ZIRFON, polysulfone, and polyphenylene sulfide), and new technological innovations in electrode and electrolyzer design were implemented.^[21,22] There are two directions of development in the industry: one is modular electrolyzers that are designed as much smaller pressurized stacks to be introduced into applications with less hydrogen demand; the second is the enhancement of single-tank hydrogen production capacity. The first single-tank

alkaline water electrolysis hydrogen production plant with a capacity of $1000 \text{ Nm}^3 \text{ h}^{-1}$ was reported in 2017, and the scale of single-tank electrolytic hydrogen production has been increased to $2000 \text{ Nm}^3 \text{ h}^{-1}$ nowadays.

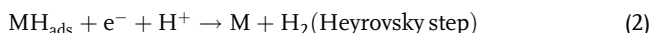
Although alkaline water electrolysis for hydrogen production has made great progress after more than 200 years of precipitation and development, it seems to be in a new “stagnation period”. The rapid development of PEMWEs shows a strong impact on the traditional water electrolysis industry. PEMWEs utilize a polymer electrolyte membrane (Nafion and Fumapem)

as a solid electrolyte instead of a diaphragm, which can effectively block electron transfer and further enhance hydrogen purity and operating current density while improving electrolyzer safety. Currently, both AWEs and PEMWEs have been successfully commercialized, and in recent years, AWEs projects have been gradually replaced by PEMs projects due to many limitations, such as low electrolytic hydrogen production efficiency, low working current density, and slow system response. Unfortunately, technological innovation regarding AWEs seems to be gradually slowing down. Meanwhile, it is challenging to further improve the electrolytic capacity for hydrogen production using existing electrodes. New technical specifications for alkaline water electrolysis for hydrogen production have been proposed by the Fuel Cells and Hydrogen Joint Undertaking in Europe, which require the development of new electrodes to achieve high current densities of 800 mA cm^{-2} by 2030.^[23] For now, there is still a long way to go. Therefore, in the face of new competitive pressures and bottlenecks, there is an urgent need to develop electrode catalysts with better catalytic activity to enhance their market competitiveness.

3. Basic Mechanistic Principles of Alkaline HER

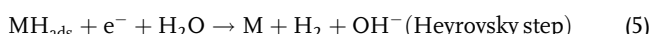
Similar to many chemical reactions, proton-coupled electron transfer plays an essential role in electrocatalytic HER processes.^[24,25] In the fundamental HER step, two-proton transfer and two-electron transfer processes will generally be involved, which is highly beneficial in proton-rich acidic media.

The HER reaction under acidic conditions is usually considered to consist of two basic steps



The first step is that a proton in solution accepts an electron and adsorbs to the reactive site; afterward, it either continues to adsorb another proton to release hydrogen, or the two adsorbed H_{ads} at the reactive site combine to form hydrogen gas.

However, in the alkaline electrolyte, the low proton concentration usually demands a water dissociation step to provide protons, which leads to a more difficult thermodynamic barrier compared to acid media. Therefore, the reaction kinetics of alkaline HER are two to three orders of magnitude slower than in acidic environments^[26]



The mechanism of HER under alkaline conditions is generally explained by two different pathways, including the Volmer–Heyrovský mechanism and the Volmer–Tafel mechanism.^[27,28] Among them, the first Volmer step is inevitable for HER, and both the Volmer step and Heyrovský step rely on the water dissociation process to provide free protons. As for the Volmer

step (Equation (4)), H^+ generated through water dissociation is adsorbed on the surface of the active site, which leads to the formation of adsorbed hydrogen (H_{ads}).^[29] The adsorbed H_{ads} can combine with another H^+ produced by water dissociation to form H_2 and desorb, known as the Heyrovský step (Equation (5)). Alternatively, two adjacent H_{ads} can also recombine to form H_2 , which is defined as the Tafel step (Equation (6)). The specific catalytic pathway and rate-determining step (RDS) of HER can usually be determined by the Tafel slope. When the Tafel slope is at a high value ($>120 \text{ mV dec}^{-1}$), it indicates that the RDS of HER is determined by the Volmer step. On the contrary, when the Tafel slope is at a low value (40 mV dec^{-1}), it usually means that the RDS is determined by the Tafel mechanism and the reaction follows the Volmer–Tafel mechanism; similarly, a Tafel slope between 40 and 120 mV dec^{-1} indicates that the Heyrovský step is the RDS and HER follows the Volmer–Heyrovský mechanism.^[30]

Due to the water dissociation, a system consisting of different ionic intermediates (i.e., H^* , OH^* , and H_2O^*) occurs in solution, which results in a far more complex mechanism of actual alkaline HER catalysis than the previous three steps. Unfortunately, the corresponding mechanisms of alkaline HER are still controversial. Among these, the widely accepted explanations include hydrogen binding energy (HBE) theory,^[31,32] water dissociation theory,^[33–35] and interface water and/or anion transfer theory.^[36] Nearly all theories still mainly focus on hydrogen adsorption or water dissociation for accelerating the kinetics of HER in alkaline media. The HBE theory aims to consider the interaction between catalysts and H^+ , simulating a reaction pathway similar to that of HER in acidic media. It was demonstrated by Yan et al. using the cyclic voltammetric curves of polycrystalline Pt as a model catalyst in electrolytes with different pH.^[31] As shown in Figure 3a,b, it could be found that the underpotential deposition (H_{upd}) peaks of hydrogen were shifted positively with the rise of pH and showed a linear relationship with the change of pH, which proves that pH is the dominant determinant of HBE. Meanwhile, it can be seen that hydrogen adsorption and hydrogen desorption are two consecutive steps occurring in HER, and there is a clear competition between them. If the catalyst surface is weakly bound to hydrogen atoms, the HER process will be difficult; conversely, when the binding strength of hydrogen atoms on catalysts is too strong, the release of H_2 cannot be achieved. The Gibbs free energy for adsorbing hydrogen (ΔG_{H^*}) can be visualized as a descriptor of the hydrogen adsorption capacity based on the HBE theory, and the HER activity of the catalysts can be further evaluated and anticipated.^[37] Based on the density functional theory (DFT) analysis, the volcanic curves were obtained by using ΔG_{H^*} , and the exchange current density (j_0), and the relationship between the catalyst and the adsorption intermediate H^* could be obtained.^[38,39] As shown in Figure 3c, ΔG_{H^*} is divided into two parts bounded by zero values. The closer the value is to zero, the better the HER catalytic activity achieves (e.g., Pt). When the value of ΔG_{H^*} is more negative, the adsorption capacity of the catalyst for H^* is stronger, which leads to the difficulty of hydrogen desorption from the catalyst surface, i.e., it is easy to affect the subsequent Heyrovský or Tafel steps in the reaction. On the contrary, the more positive the value of ΔG_{H^*} , the weaker the hydrogen adsorption capacity of the catalyst, which has a greater impact on the Volmer step.^[39] However, in the actual alkaline HER, besides H^+ , there are many reaction intermediates (such as OH^* and H_2O^*) as participants in

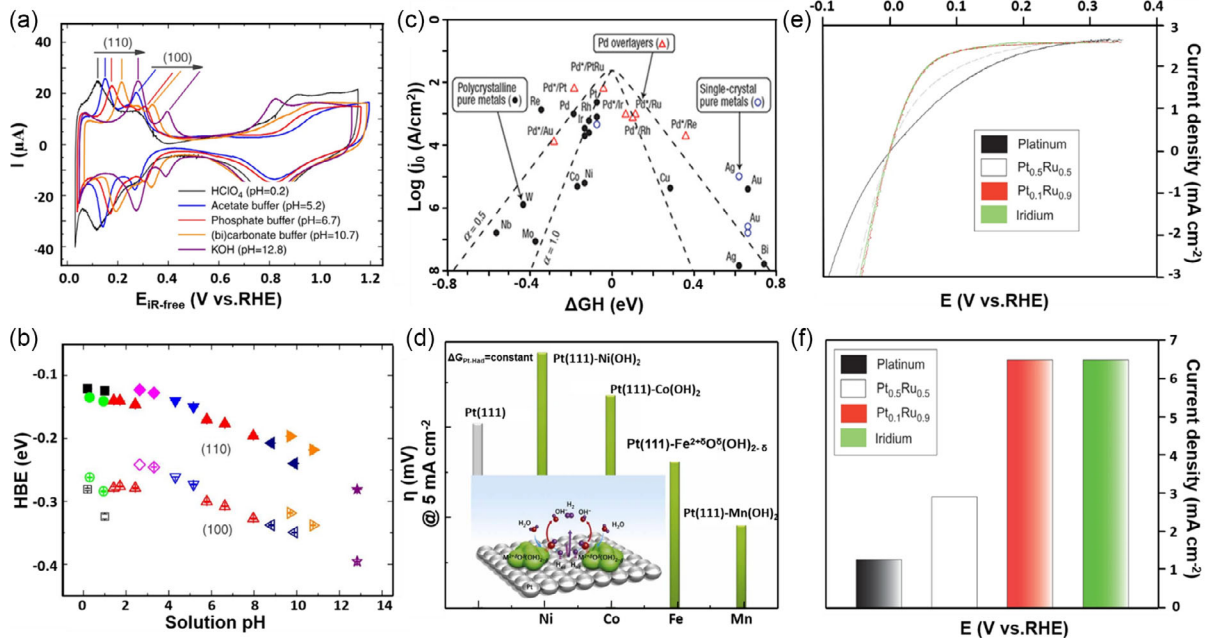


Figure 3. a) Cyclic voltammetric curves (CV) showing hydrogen adsorption/desorption peak positions (HUPD) at different pH electrolytes.^[31] b) Variation curve of HBE value with pH value. Reproduced with permission.^[31] Copyright 2015, Springer Nature. c) Volcano plot of ΔG_{H^*} values for different metals. Reproduced with permission.^[39] Copyright 2022, Wiley-VCH GmbH. d) Comparison of the overpotential of different metal oxides in concert with Pt. Bottom left inset: HER Catalytic mechanism under synergistic interaction. Reproduced with permission.^[33] Copyright 2012, Springer Nature. e) HOR/HER polarization curves of PtRu alloys.^[40] f) “Kinetic current” for PtRu alloys. Reproduced with permission.^[40] Copyright 2013, Springer.

the reaction, which are not considered in the volcano diagram, so the volcano diagram based on ΔG_{H^*} values cannot provide enough guidance. The water dissociation theory takes into account the OH* produced during the water dissociation process. As a classic example, Figure 3d shows that if Ni(OH)₂ is introduced onto the Pt active site as an OH_{ad*} adsorption site, it effectively promoted water dissociation and prevented “poisoning” with OH_{ad}, which effectively facilitates the Volmer step.^[33] Likewise, Markovic et al. greatly enhanced the HER activity of the catalyst in alkaline environment by introducing Ru sites into Pt as oxophilic elements to provide sites for OH_{ad} (Figure 3e,f).^[40]

In addition to ΔG_{H^*} , d-band center theory is often used to predict the adsorption capacity of H* on catalysts. The localized metal d electrons at the metal sites will be involved in the formation of M–H bonds.^[39,41] When the 1s orbital of H* hybridizes with d orbital of the metal, the filled bonding states and the partially occupied antibonding state will be formed.^[39] The higher the occupancy of the antibonding state, the weaker the bonding strength of M–H. As the d-band center of the active site gets closer to the metal Fermi energy level, it generates a higher σ* energy level and stronger H* adsorption.^[14] As previously mentioned, the adsorption energy of the active site for H* should be appropriate, so obtaining the right metal d-band center is essential for designing excellent HER catalysts.

Numerous theories have been applied to the design of alkaline HER catalysts. The core of the design depended on optimizing the reaction thermodynamics to reduce the water dissociation energy barrier on the one hand or modulating the hydrogen adsorption capacity on the catalyst surface to facilitate the effect

of reaction kinetics on the other. Based on the high current density reaction conditions required in industrial environments, the performance of the catalyst is also extremely demanding, so it is of great importance to optimize the three reaction steps according to the mechanism to improve the reaction kinetics.

4. Design Challenges of HER Electrocatalysts in Industrial Applications

Based on the high current densities and high stability required in industrial environments, the design of electrocatalysts is still far more demanding than that under laboratorial conditions. Therefore, in the context of considering the industrial operating environment and the HER reaction mechanism, this section summarizes the challenges of HER electrocatalyst design under industrial conditions from both a microscopic and macroscopic perspective.

4.1. Challenges at the Microscopic Scale

4.1.1. Modulation of the Interface

The catalytic activity and stability of catalysts are highly related to charge transfer capability. In the field of electrocatalysis, there are generally two steps in electron transport and charge transfer: 1) migration from the conductive support to the catalyst; and 2) participation in the adsorption and desorption of reaction intermediates at the catalyst surface. In these two steps, it is

inevitable that both conductive support-catalyst and catalyst-electrolyte interfaces will be involved.

The selection of a suitable conductive substrate can optimize the conductivity in the electrode system and reduce the ohmic resistance loss inside the electrode. Commonly, there is often a huge ohmic loss between the support and the catalyst, which affects the performance of the catalyst. While the interface between the conductive substrate and the catalyst can be effectively optimized for electron transfer in most metal substrates, such as metal mesh, metal foam, and so on. Chhowalla et al. investigated the effect of electrical coupling between catalyst

and substrate on catalytic performance by constructing MoS₂ electrochemical microcells (Figure 4a).^[42] As shown in Figure 4b,c, MoS₂ was deposited and tested on different substrates with different contact resistances. It was found that a substantial decrease in current density and the turnover frequency (TOF) of MoS₂ occurred as the contact resistance increased. The previous study indicates that the reduced contact resistance facilitates the charge injection from the substrate into the catalyst, which leads to a significant improvement in the catalytic performance. In addition to the selection of a suitable conductive substrate, using conductive materials as “relay stations” for charge transfer to reduce the

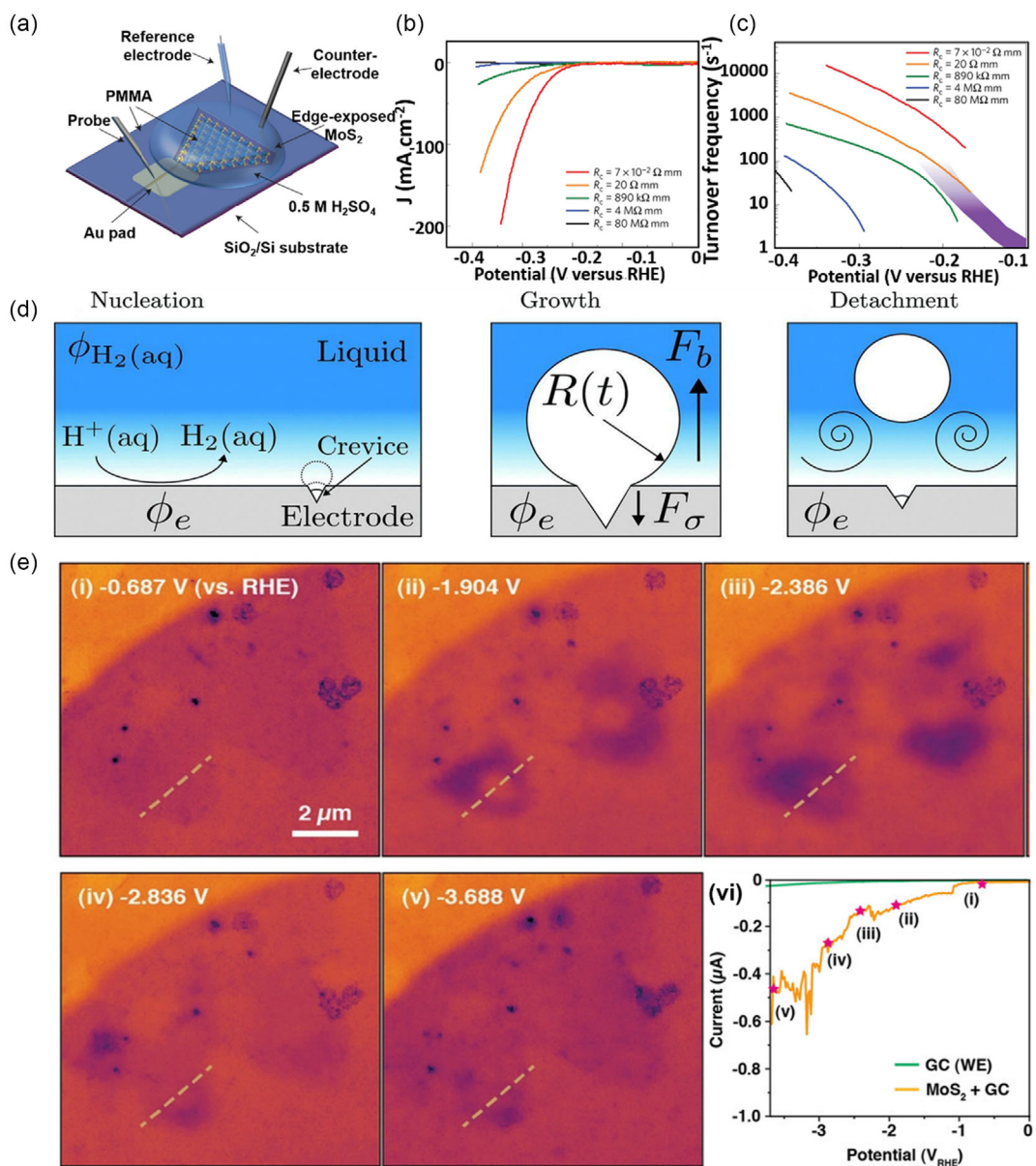


Figure 4. a) Schematic diagram of MoS₂ electrochemical microcell device.^[42] b) Current density polarization curves and c) the turnover frequency (TOF) of MoS₂ microcells with different contact resistances. Reproduced with permission.^[42] Copyright 2016, Springer Nature. d) Bubble nucleation, growth and desorption processes on electrodes. Reproduced with permission.^[54] Copyright 2008, The Royal Society of Chemistry. e) (i–v) In situ time-resolved LPTEM images at different potential; (vi) Corresponding LSV curve. Reproduced with permission.^[56] Copyright 2022, Wiley-VCH GmbH.

charge transfer limitations of the conductive substrate and active center is another strategy. For example, the conductivity of the catalysts can be enhanced by physically mixing with a certain amount of carbon black in the ink solutions.^[43] Alternatively, the charge transfer kinetics can be enhanced by coupling with a conductive material.^[44–46] Dang et al. preferentially utilized MXene ($Ti_3C_2T_x$) modification on nickel foams, which greatly improves the performance of electrodeposited cobalt phosphate due to the good electrical conductivity and fast ion transport structure of MXene.^[46]

As optimization based on catalyst support is often limited by the demand for decreasing electrode costs in industrial production, researchers pay much attention to controlling the catalyst-electrolyte interface. As mentioned in Chapter 3, the HER electrocatalytic process involves three consecutive steps: adsorption, activation, and desorption. Compared with the restricted adsorption and desorption of reaction intermediates that are common for single-component catalysts, the inclusion of multiple active components at the catalyst interface generates a synergistic effect that modifies the normal arrangement of atoms to increase electron transport and charge transfer, which creates more active centers than single components. Therefore, through the rational design of the interfacial structure on the electrocatalyst, electron transfer can occur rapidly between the adsorbed intermediate and the catalyst, improving the catalytic performance of HER. The high current density reaction conditions based on industrial electrolysis for hydrogen production imply the presence of more active charge transfer, which also suggests that it is a great challenge to establish a suitable catalyst interface to promote charge transfer to the reaction intermediate.

4.1.2. Rational Design Geometric Structure of the Electrocatalyst

To construct HER electrocatalysts that satisfy the criteria for commercial applications, it is essential to design a reasonable geometric structure of electrocatalysts at the microscopic scale. Designing the microscale geometric structure can improve the density and intrinsic activity of the active sites by the morphological geometric structure of the material and the local geometric structure of the active sites, respectively.

Under the high current density requirements of commercial electrolytic hydrogen production, introducing more active sites in the same electrode area can effectively boost the reaction rate and achieve higher current densities at lower overpotentials.^[47] The multidimensional morphological geometry is designed at the microscopic scale, which is beneficial to increase the specific surface area of the catalyst and thus expose more active sites to enhance the catalytic properties.^[48] Sun et al. demonstrated that the construction of nanostructured films with rich multidimensional structure can generate broken contact lines at the gas–liquid–solid interface, potentially increasing catalytic activity by reducing bubble adhesion and promoting electrolyte penetration.^[49]

The design of the geometric structure of the active site is another focus in designing the electrocatalyst structure. As is well known, in the electrocatalytic process, the real catalytically active sites may be single atoms or localized structures composed of several atoms. While other atoms around the active site assume the role of modulating the electronic effects of the active site,

which complement the real active site.^[50] As mentioned earlier, the electronic structure distribution determines the adsorption and desorption capacity of the reaction intermediates, which in turn affects the catalytic activity. Therefore, the optimization of the tuning of the geometric structure of the active component will determine the true intrinsic activity of the active site.^[51] Currently, various methods, such as defects, strain, doping, and heterostructures, are used to tune the geometric structure around the active site. Although several progresses have been achieved in related research, the lack of precise modulation at the nanoscale and the development of characterization tools still prevent the optimal design of the geometric structure of the active site. In conclusion, the design of electrocatalyst geometric structures still needs further exploration.

4.2. Challenges at the Macroscopic Scale

4.2.1. Deactivation of Catalyst

To fulfill the criteria for industrial applications, the stability of the catalyst becomes a topic that must be discussed. Sometimes catalysts have excellent catalytic activity, but deactivation always becomes evident within a certain time period, thereby hindering the commercial viability of the catalyst. Industrial AWEs are generally large-scale and difficult to install, so the electrolyzers were expected to steadily produce hydrogen at an enough long period (5–10 years) without disassembling to replace electrodes. Raney nickel is widely recognized and used for industrial production applications because of its good stability. Under an ampere-level current density condition, electrocatalysts need to be operated in extreme environments far from the equilibrium potential. Fourteen modes of catalyst deactivation processes have been summarized by Pérez-Ramírez et al., in which they mentioned a tendency for the catalyst to agglomerate during electrocatalysis or loss of active phase in the reaction mixture (expressed as depletion), accompanied by unfavorable changes in electronic properties.^[52] In addition, the deactivation of catalysts would be speeded up because of the large amount of charges transfer in industrial operating environments. Moreover, the high alkalinity of the industrial electrolyte can also affect the stability of the electrocatalysts severely.^[53] In summary, more efforts should be made to optimize the stability of commercial catalysts.

4.2.2. Bubble Effect on the Surface

The formation and release of bubbles are prevalent phenomena in gas evolution reactions, which affect the overall energy input and mass transport (Figure 4d).^[54] Due to the formation of the gas–liquid–solid interface, the release of H_2 gas at the nonhomogeneous active site may cause kinetic perturbations.^[55,56] Under low current densities, H_2 is allowed to diffuse into the native electrolyte before the concentration threshold for bubble nucleation due to the limited H_2 production rate. In contrast, under high current densities, the rate of bubble generation is much higher than the rate of H_2 desorption from the surface, which results in a large amount of bubble accumulation on the catalyst surface. In this case, the active sites on the surface are blocked by the bubbles, which results in uneven current density distribution,

electrolyte-catalyst contact, and mass transfer.^[54] Park et al. observed the kinetic separation of H₂ bubbles on the MoS₂ surface by *in situ* electrochemical liquid-phase transmission electron microscopy (LPTEM) in real time (Figure 4e).^[56] It was found that the linear sweep voltammetry (LSV) curve fluctuated sharply due to the adsorbed bubbles-induced local inhibition of mass transfer, which causes clogging of the electrolyte molecules at the interface. Modestino et al. investigated the complex dependence between the bubble evolution process and electrochemical phenomena and revealed a dynamic evolution of the ohmic overpotential during bubble growth, which in turn leads to an increase in ohmic resistance due to the blocking of the ionic path of current transport.^[57] Meanwhile, Bao et al. demonstrated that the external bubble detachment could have a great influence on the ion transport inside the electrode by building a two-phase mathematical model.^[58] In addition, at high current densities, bubbles are generated on the electrode surface in the form of thermal evolution. This phenomenon of heat loss is called the “water anode effect”.^[59]

In industrial applications, mechanical circulation of the electrolyte is often used to reduce the effect of bubbles on the electrolytic efficiency, which can accelerate the detachment of air bubbles.^[60] Although this approach can address the effects of bubble retention to some extent, bubbles can still generate a “gas blanket” between the electrode and the diaphragm and may cause complicated local convection of the electrolyte, which causes additional overpotential losses.^[61–63] Shen et al. used a 3D computational fluid dynamics model to study the transient bubble behavior in a commercial AWE. They found that bubbles would form bubble plugs within the flow channel, which had a significant negative impact on the electrolyzer’s performance. Meanwhile, the generation of bubbles has a great impact on the mass flux of the electrolyte, which leads to an uneven distribution of the electrolyte on the electrode surface and a consequent decrease in the electrolysis rate of water.^[64] Vreman et al. also performed a numerical simulation of the secondary current distribution in the most advanced “zero-gap” electrolyzer, which showed that the presence of bubbles contributes to a certain degree to the increase in resistance.^[65] Furthermore, the presence of nanobubbles (0.15 μm) in the diaphragm pores has the potential to affect the diaphragm resistance and is also responsible for additional ohmic resistance loss.^[62,65] Moreover, the high-speed flow system also adds more challenges to the durability of the electrodes and devices. The study by Manabe et al. reported that a large amount of trapped gas would lead to the deterioration of the electrolyzer device.^[66]

The bubble problem will also have an impact on the mechanical stability of the electrocatalysts. In laboratory testing equipment, powdered catalysts are often attached dropwise to conductive substrates, which are often at risk of falling off. As the bubbles on the electrode are generated from the inside out and start from small to large, the intense bubbles at high current densities often make electrocatalysts peel off from the conductive substrate, which causes severe damage to the catalyst layer or leads to structural collapse, finally degrading the HER performance of the electrodes.^[67] Therefore, it is essential to further improve the bubble kinetics during the gas evolution reaction when designing electrocatalysts.

4.2.3. Large-Scale Fabrication

Despite the great progress made on the design of HER catalysts, the “gap” between laboratory and industrial hydrogen production still exists. The synthesis method is the biggest obstacle to bring electrocatalysts from laboratory to industrial applications. Although many catalysts have excellent catalytic performance and stability, the synthesis process is usually either too complex (high cost) or not easily scalable (low yield). Currently, Raney nickel is commonly used as a catalyst in commercial AWEs and is loaded onto alloy steel grids by high-temperature plasma spraying (PS) techniques. Although the process is relatively mature, there are still problems, such as uneven loading, high plasma power consumption, and easy dust pollution. Therefore, a new synthesis process for catalysts in large quantities and on a large scale is also imminent at the macroscopic scale.

5. Microscopic Design Strategies for HER Electrocatalysts to Enhance Intrinsic Activity

As mentioned, improving catalytic activity and overcoming catalyst deactivation are the main challenges in designing industrial HER electrocatalysts. Various approaches have been proposed to enhance electrocatalytic performance, including optimization of active site’s electronic structure, construction of active interfaces, and construction of dual active sites. Here, we summarize these design strategies and corresponding electrocatalysts up to now (Table 2).

5.1. “Mutual Help”: Optimization of the Active Site’s Electronic Structure to Break the Catalytic Limits

The catalytic activity of HER is closely related to intermediate adsorption and desorption, as well as the breaking and formation of chemical bonds. As shown in the volcano diagram, there are limitations on the HBE of single-component catalysts. Therefore, to break the general linear relationship, some other components tend to be introduced, which can modulate the charge distribution and charge transfer ability within the catalyst. Here, several more effective design strategies to modulate the electronic structure of catalysts are summarized, such as doping, defect engineering, and the construction of heterostructures.

5.1.1. Doping

The difference in charge distribution between doped atoms and active sites shows potential for optimizing the electronic structure of the active sites, which will regulate the adsorption of intermediates.^[68]

The doping of a small concentration of metals may cause a change in the electronic structure of the active site, which leads to the easier generation of the high-valence metal state as the active site and optimizes the adsorption energy.^[69,70] Transition metal elements are often used in cation doping strategies. Yang et al. used DFT to calculate the Gibbs energy of adsorbed hydrogen (ΔG_{H^*}). The doping of Fe significantly reduced the ΔG_{H^*} to -0.01 eV near the top of the volcano compared with pure N₂P, which greatly facilitated the hydrogen conversion kinetics

Table 2. Summary of excellent HER electrocatalysts by enhancing intrinsic activity.

Strategy		Catalyst ^[ref.]	Electrolyte	Overpotential (mV@500 mA cm ⁻²)	Overpotential (mV@1000 mA cm ⁻²)	Stability
Optimization of active site's electronic structure	Doping	Fe-doped Ni ₂ P ^[51]	1 M KOH	≈100	183	/
		F _x C ₁ CH/NF ^[72]	1 M KOH	246	256	100 mA cm ⁻² for 136 h
		Sn–Ni ₃ S ₂ /NF ^[73]	1 M KOH	≈400	579	≈200 mA cm ⁻² for 60 h
		V-Ni ₅ P ₄ ^[74]	1 M KOH	/	295	≈140 mA cm ⁻² for 48 h
		F-Co ₂ P/Fe ₂ P/IF ^[75]	1 M KOH	229.8	260.5	2000 mA cm ⁻² for 10 h
			6 M KOH	≈200	≈243	/
		Pt/8-NCNT ^[78]	1 M KOH	107	153	500 mA cm ⁻² for 100 h
		NC/Ni ₃ Mo ₃ N/NF ^[79]	1 M KOH	500 (668 mA cm ⁻²)	954 (1500 mA cm ⁻²)	1100 mA cm ⁻² for 50 h
		N–NiMoS ^[80]	1 M KOH	250	322	≈20 mA cm ⁻² for 720 h
		A-NiCo LDH/NF ^[81]	1 M KOH	286	381	360 mA cm ⁻² for 50 h
Creating defects		Se-Ps ^[29]	1 M KOH	261 (400 mA cm ⁻²)	/	100 mA cm ⁻² for 800 h
		Pt SAs/MoO ₂ NRs ^[83]	1 M KOH	≈600	/	500 mA cm ⁻² for 100 h
		MoNi ₄ /MoO _{3-x} ^[85]	1 M KOH	114	156	/
		CoMoS _x ^[87]	1 M KOH	269	/	500 mA cm ⁻² for 100 h
Heterostructure engineering		CoF ₂ ^[88]	1 M KOH	251 (400 mA cm ⁻²)	365 (1200 mA cm ⁻²)	10 mA cm ⁻² for 110 h
		NiMoO _x /NiMoS ^[89]	1 M KOH	174	236	500 mA cm ⁻² for 500 h
		MoS ₂ /Ni ₃ S ₂ NW-NF ^[90]	1 M KOH	182	200	1000 mA cm ⁻² for 12 h
		Nir 12 ₂ -450 NWs/CC ^[91]	30 wt% KOH	≈625	≈1190	1000 mA cm ⁻² for 40 h
		R–CoC ₂ O ₄ @MXene ^[92]	1 M KOH	157	216	1000 mA cm ⁻² for 100 h
		FeP/Ni ₂ P ^[93]	1 M KOH	≈210	≈275	500 mA cm ⁻² for 40 h
		CoP@Ni ₂ P ^[94]	1 M KOH	209	/	500 mA cm ⁻² for 48 h
Interface interaction		1T _{0.63} –MoSe ₂ @MoP MPIC ^[95]	1 M KOH	≈225	358	1000 mA cm ⁻² for 100 h
		NFCH–NMO ^[99]	1 M KOH	297	/	500 mA cm ⁻² for 80 h
		sc-Ni ₂ P ^δ /NiHO ^[100]	1 M KOH	≈187 (400 mA cm ⁻²)	/	10 mA cm ⁻² for 100 h
		Ni ₅ P ₄ –Co ₂ P ^[101]	1 M KOH	199	267	250 mA cm ⁻² for 100 h
		Co–Mo ₅ N ₆ ^[104]	1 M KOH	≈250	280	1000 mA cm ⁻² for 10 h
		Co ₄ N–CeO ₂ ^[105]	1 M KOH	190	/	200–500 mA cm ⁻² for 60 h
		RuO ₂ –NiO ^[109]	1 M KOH	100 (452 mA cm ⁻²)	≈150	100 mA cm ⁻² for 20 h
Dual active sites		Sr ₂ RuO ₄ ^[111]	1 M KOH	/	278	1000 mA cm ⁻² for 35 days
		GDY/MoO ₃ ^[113]	0.1 M KOH	/	1800 (1200 mA cm ⁻²)	100 mA cm ⁻² for 24 h
		Cu–FeOOH/Fe ₃ O ₄ ^[115]	1 M KOH	285	349	100 mA cm ⁻² for 100 h
		Ni–W ^[116]	1 M KOH	303	/	/
		P–Fe ₃ O ₄ ^[117]	1 M KOH	200 (409 mA cm ⁻²)	≈247	100–500 mA cm ⁻² for 60 h
		Cor 60h cm ^[118]	1 M KOH	/	165 (1000 mA cm ⁻²)	1000 mA cm ⁻² for 20 h
					220 (2000 mA cm ⁻²)	
		Ru–Ni ₂ P/NiO/NF HNSs ^[119]	1 M KOH	/	112	20 mA cm ⁻² for 100 h
		Ni ₃ N@2M–MoS ₂ ^[120]	1 M KOH	299	327	1000 mA cm ⁻² for 300 h
		Ni ₂ P/WO _{2.83} ^[121]	1 M KOH	/	254.5	1000 mA cm ⁻² for 50 h
Enhancing surface area		WP–W ₂ C ^[122]	1 M KOH, 25 °C	375 (570 mA cm ⁻²)	560	1000 mA cm ⁻² for 60 h
			1 M KOH, 70 °C	/	449	100 mA cm ⁻² for 21 h
			5 M KOH	/	425 (1000 mA cm ⁻²)	/
					780 (2000 mA cm ⁻²)	
		Fe@Fe _x NiO/Ni@Ni _y CoP ^[123]	1 M KOH	/	129 (1500 mA cm ⁻²)	100 mA cm ⁻² for 100 h
Improving electron transfer		Ni ₃ S ₂ /Cr ₂ S ₃ ^[116]	1 M KOH	/	277 (1000 mA cm ⁻²)	1000 mA cm ⁻² for 25 h
					246 (3000 mA cm ⁻²)	
					251 (3500 mA cm ⁻²)	

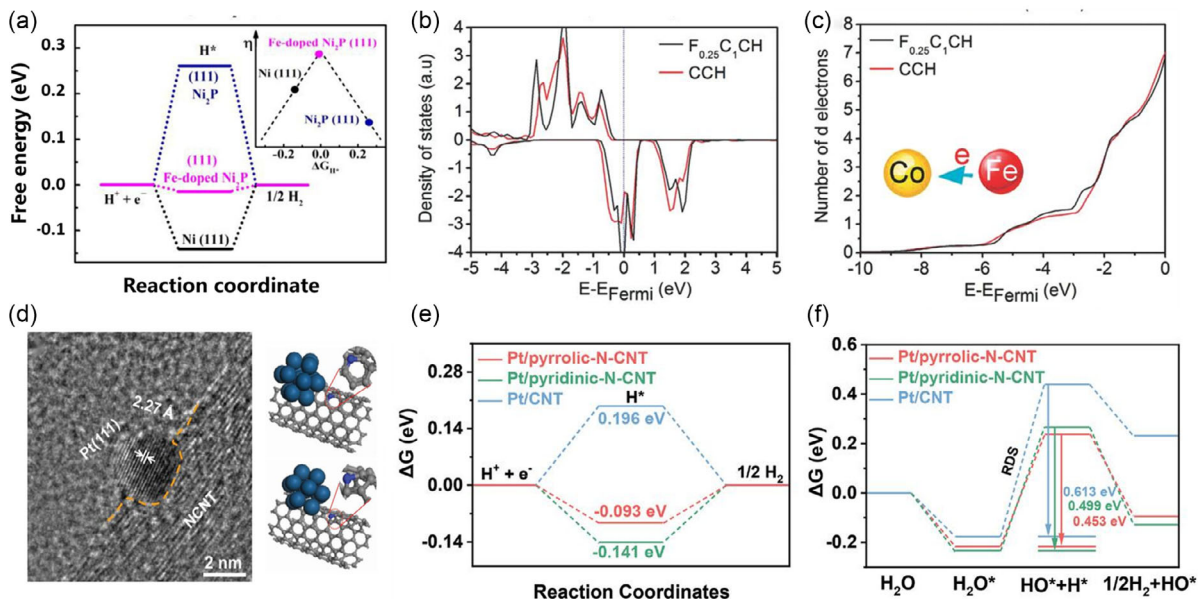


Figure 5. a) Changes in ΔG_{H^*} value of Ni_2P after Fe doping. Reproduced with permission.^[71] Copyright 2019, American Chemical Society. b) DOS of Co 3d orbitals and c) the difference in electron numbers of Co atoms in 3d orbitals after Fe doping. Reproduced with permission.^[72] Copyright 2018, Wiley-VCH GmbH. d) HRTEM image and theoretical model of Pt/8-NCNT.^[78] e) ΔG_{H^*} value and f) Gibbs free energy diagram of HER steps for different N-doped Pt/CNT. Reproduced with permission.^[78] Copyright 2022, Wiley-VCH GmbH.

(Figure 5a).^[71] Benefiting from the influence of Fe, the Fe-doped NF@ $\text{Fe}_2\text{-Ni}_2\text{P}/\text{C}$ exhibited an excellent HER catalytic activity ($\eta_{1000} = 183$ mV). In addition, Li et al. designed Fe-doped Co carbonate hydroxide nanosheets (NSs) arrayed on 3D conductive Ni foam (FCCH/NF) with different contents of Fe, which effectively modified the electrocatalyst morphology to offer more active sites.^[72] Meanwhile, the doping of Fe decreases the energy of Co atoms, which leads to an increase in the number of 3d orbital electrons of the Co atom, thus making it easier to adsorb hydrogen protons (Figure 5b,c). Many studies have shown that the introduction of metal elements with a higher valence state into the catalysts is more likely to accelerate the electron migration rate. For instance, Feng et al. successfully doped Sn^{4+} into Ni_3S_2 . With Sn dopant as an electron acceptor, partial electron transfer of metallic Ni accelerated to generate more Ni^{2+} , and thus $\text{Sn-Ni}_3\text{S}_2/\text{NF}$ showed remarkable HER activity with 579 mV at 1 A cm^{-2} .^[73] The V- Ni_5P_4 prepared by Yi et al. achieved an ultra-high current density in the amperometric range with an overpotential of only 295 mV, which is attributed to the electron redistribution of Ni_5P_4 due to V doping, making the hydrogen more favorable to the P site for Ni–Ni–V.^[74]

Anion tuning strategies are no less significant than metal cation doping. Most anionic components are more electronegative than transition metals. F is often used as a dopant to effectively tune the electronic structure due to its highest electronegativity. Chai's group used F-doped CoFe Prussian blue analogs to synthesize fluorine-doped iron cobalt phosphide nanocubes (F- $\text{Co}_2\text{P}/\text{Fe}_2\text{P}/\text{IF}$), which achieved excellent catalytic performance for HER ($\eta_{1000} = 260.5$ mV).^[75] Due to the huge difference in electronegativity between F and S atoms, the introduction of F element into Ni_3S_2 (F- Ni_3S_2) can synergistically optimize the

Ni active site, making it exhibit excellent HER performance (300 mA cm^{-2} at about -0.225 V vs RHE).^[76] N doping is frequently used to modify carbon support, which has been proposed to have synergistic effects in improving HER activity.^[77] Wang et al. anchored Pt on N-doped carbon nanotubes (CNT) as an excellent HER catalyst, performing stable hydrogen production for 100 h at 500 mA cm^{-2} (overpotential of 107 mV).^[78] The excellent stability is attributed to the strong metal-support interaction of the N-doped CNT, which allows the Pt nanoparticles to be uniformly dispersed on the CNT surface (Figure 5d). The interaction between pyridine-N and Pt generated by doping both promotes the adsorption and accelerates the dissociation of water, which results in an excellent catalytic activity (Figure 5e,f). Zhou's group proposed a dicyandiamide pyrolysis method to synthesize NC/ $\text{Ni}_3\text{Mo}_3\text{N}/\text{NF}$ by successfully coating a nitrogen-doped carbon on a NiMo_3N surface. Impressively, the HER current density of NC/ $\text{Ni}_3\text{Mo}_3\text{N}/\text{NF}$ at 500 mV overpotential (668 mA cm^{-2}) is nearly twice as high as that of 20 wt% Pt/C (379 mA cm^{-2}).^[79] This excellent performance is attributed to N doping, in which catalytic material transforms into a metal-semiconductor structure that has a suitable ΔG_{H^*} on different active sites. Moreover, Yu et al. introduced N into the NiMoS precursor.^[80] The doping of N effectively modulated the electron density and shifted the d-band center of NiMoS , which conferred N- NiMoS better HER catalytic activity than pure NiMoS (1000 mA cm^{-2} at -0.322 V vs RHE). Nonmetallic doping can also lead to the creation of amorphous structures or crystal distortions, which can produce more active sites. In this regard, Wu et al. doped NiCo crystalline layered double hydroxides (NiCo LDH/NF) with a small amount of B elements, which endows LDH with an amorphization structure (A-NiCo LDH/NF). Consequently, A-NiCo LDH/NF obtained a superior performance of 1000 mA cm^{-2} at 0.381 V

versus RHE.^[81] In addition to exposing more active sites, the amorphous structures with abundant unsaturated atoms and O vacancies increase the local electron density. Although rarely mentioned, Se doping also makes an outstanding contribution to HER activity enhancement. Lei's group successfully enhanced the electron transfer between the skin-core structures nanoarrays by Se doping, which further optimizes the HER performance of the catalyst (400 mA cm^{-2} at 0.261 V versus RHE).^[29]

The doping strategy is not restricted to a single-element doping; the multielement codoping approach allows for more precise modulation of the electronic state of the catalytic active site. For instance, Li et al.^[69] adjusted morphological structure and electronic properties by systematically adjusting the doping ratios of P and S elements in the $\text{FeCoNiP}_x\text{S}_y$ catalyst, finally reaching a current density of 1000 mA cm^{-2} at a low overpotential of 264 mV in 1 M KOH .

5.1.2. Creating Defects

According to the second law of thermodynamics, the arrangement of atoms is not as complete and regular as it should be due to the circumstances surrounding crystal formation and atoms' thermal motion, which invariably results in flaws that

depart from the ideal crystal structure. These defective sites usually tend to trigger the electron distribution structure of the local sites around them, bringing unique catalytic activity to the catalyst.^[82,83] One of the common types of defects is oxygen vacancies, which can be used to narrow the bandgap to construct unsaturated sites for optimizing the active center. Meanwhile, oxygen defects can be used to modify or anchor metal atoms due to the excellent ability to tune the electronic structure, which enhances the strong interactions between the loaded metal phase and the carrier. Following it, Guo et al. synthesized Pt single-atom catalysts anchored on MnO_2 nanorods (Pt SAs/ MoO_2 NRs). As shown in Figure 6a, a large amount of Pt SA is strongly anchored at oxygen vacancy sites, which delivers a high current density of -500 mA cm^{-2} with an overpotential of only $\approx 600 \text{ mV}$ for HER (Figure 6b).^[83] Especially, it also maintains a stable long-term stability of 100 h at 500 mA cm^{-2} . Based on the results of DFT calculations, the electronic state of the active site (Pt) was optimized for optimum hydrogen desorption energy (ΔG_{H^*}) and water dissociation energy. It has been widely confirmed in recent years that MoO_3 can effectively increase HER activity by creating oxygen vacancies.^[84] Based on this, Hu's group synthesized $\text{MoNi}_4/\text{MoO}_{3-x}$ nanorod array electrodes using a thermal reduction strategy.

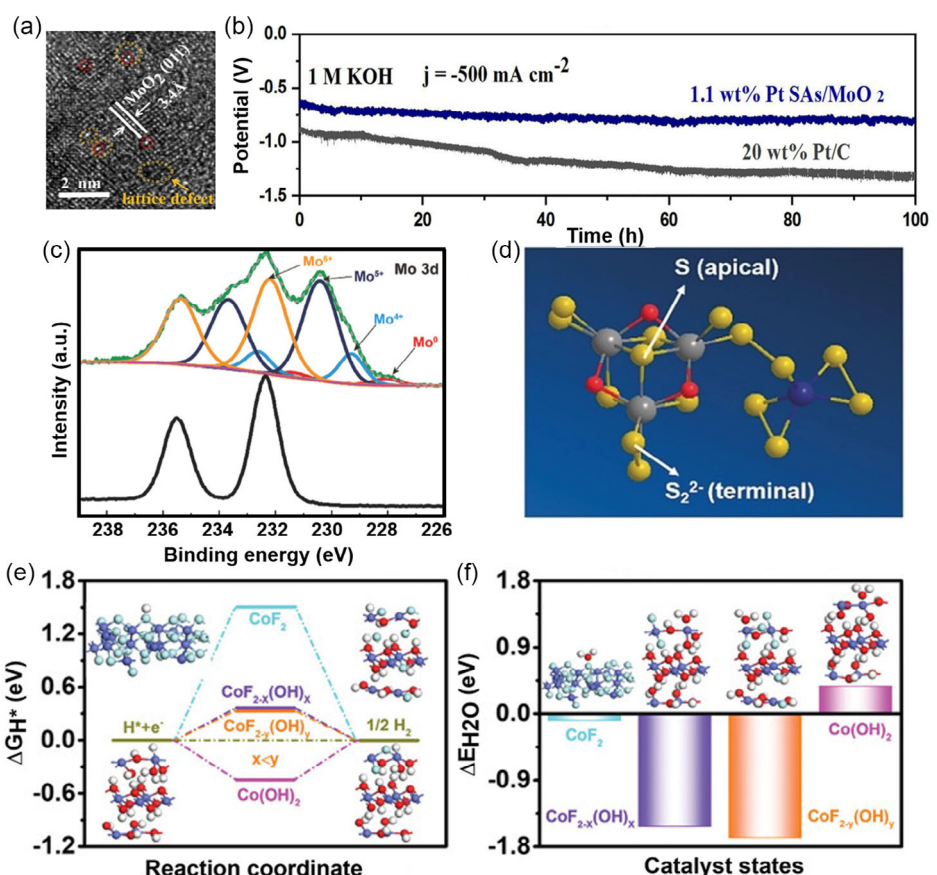


Figure 6. a) TEM images of Pt SAs/ MoO_2 (red circles represent Pt SAs and yellow circles represent oxygen vacancy defects).^[83] b) HER stability curves of 1.1 wt% Pt SAs/ MoO_2 and 20 wt% Pt/C in 1 M KOH. Reproduced with permission.^[83] Copyright 2022, Elsevier. c) Mo 3d XPS spectra of NiMoO_4 (black) and $\text{MoNi}_4/\text{MoO}_{3-x}$. Reproduced with permission.^[85] Copyright 2017, Wiley-VCH GmbH. d) Model structure of CoMoS_x constructed based on experimental results (defined as $\text{Mo}_3\text{S}_{10}\text{O}_3\text{-CoS}_5$). Reproduced with permission.^[87] Copyright 2019, Wiley-VCH GmbH. e) ΔG_{H^*} and f) $\Delta E_{\text{H}_2\text{O}}$ of different structure models. Reproduced with permission.^[88] Copyright 2021, Wiley-VCH GmbH.

The presence of low-valence Mo in X-ray photoelectron spectroscopy (XPS) implies the presence of MoO_{3-x} with oxygen vacancies (Figure 6c).^[85] Benefiting from the presence of oxygen vacancies, $\text{MoNi}_4/\text{MoO}_{3-x}$ has a much lower R_{ct} compared to the controlled sample, thereby exhibiting HER catalytic activity in 1 M KOH with commercial application potential ($\eta_{1000} = 156 \text{ mV}$).

Amorphous materials typically have more defects than crystalline materials.^[86] Jiang et al. successfully designed an amorphous CoMoS_x catalyst that delivered a high current density of 500 mA cm^{-2} at a low overpotential of 269 mV .^[87] A comparison of the experimental K-edge X-ray absorption near-edge structure (XANES) and theoretical spectra of CoMoS_x revealed that the CoMoS_x structure contains a large number of defects, favoring more active site exposure (Figure 6d). Mu's group proposes a self-reconstruction strategy based on the leaching of F^- to construct porous and defective interwoven NSs interconnected by $\beta\text{-Co(OH)}_2$ nanoparticles.^[88] During reconstruction, the catalyst is first converted from CoF_2 to an amorphous NS interwoven structure with a large number of $\beta\text{-Co(OH)}_2$ structural defects and then to a low-crystallinity NP. The resultant ultrasmall and defective nanostructures contribute to a significant reduction in ΔG_{H^*} .

and water adsorption energy, thus providing favorable kinetics for the HER process (Figure 6e,f).

5.1.3. Engineering Heterostructures

Heterogeneous structures are generally composed of multiple substances. Electron interaction between multiple substances in the heterostructure reduces the reaction energy barrier at the active site, which can further enhance the reaction thermodynamics and kinetics of the catalyst. The Hou's group has synthesized a $\text{NiMoO}_x/\text{NiMoS}$ heterostructure array by oxidation/hydrogenation-induced surface synthesis using NiMoS precursors, which keep stable at a high current density of 500 mA cm^{-2} over 50 h operating at an ultra-low overpotential of 174 mV .^[89] DFT calculations demonstrated that the excellent catalytic activity of $\text{NiMoO}_x/\text{NiMoS}$ originates from the multi-interfacial composition of the electron distribution in the heterostructure, which creates a unique S-H adsorption site and thus avoids the excessively strong adsorption of H^* (Figure 7a). Long and dense heterogeneous structured nanowires ($\text{MoS}_2/\text{Ni}_3\text{S}_2$ NW-NF) were constructed, not only enabling the synergistic

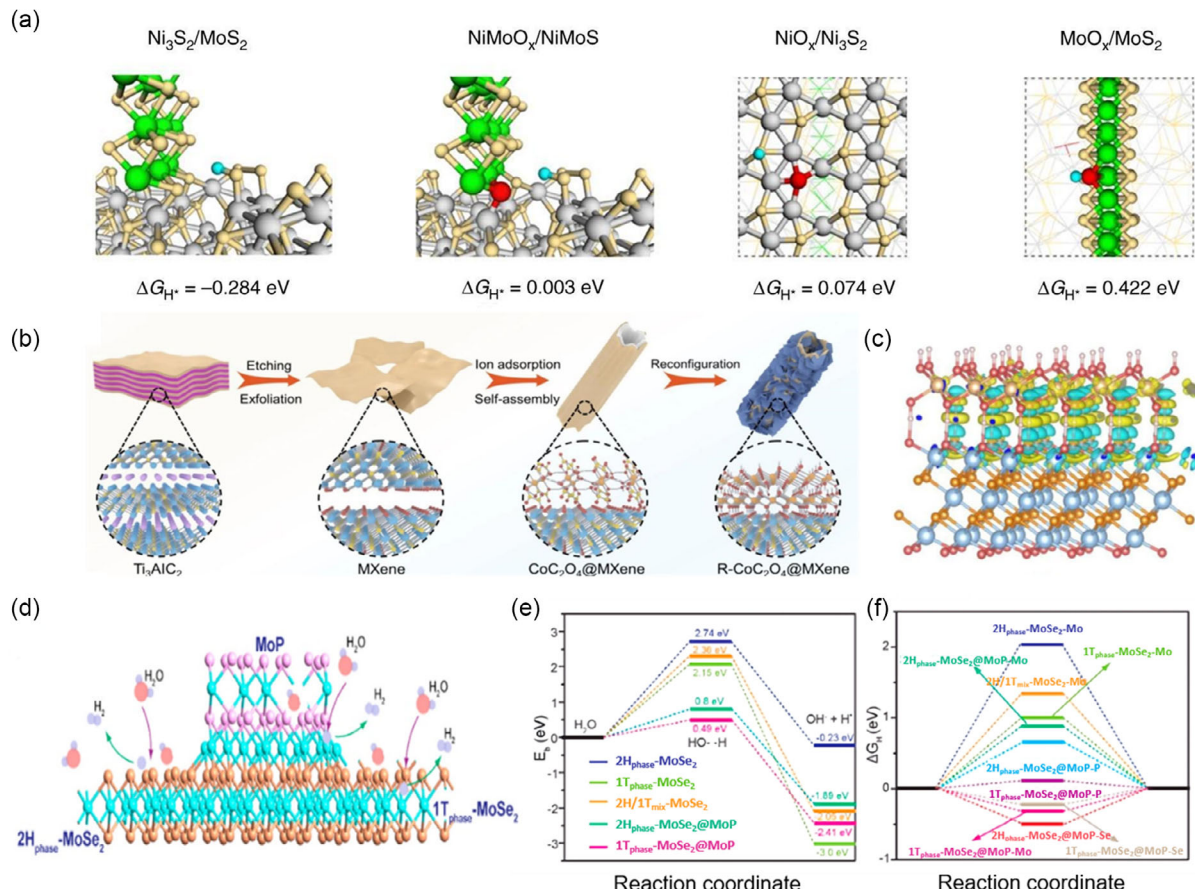


Figure 7. a) Hydrogen adsorption model and the corresponding ΔG_{H^*} of $\text{Ni}_3\text{S}_2/\text{MoS}_2$ and $\text{NiMoO}_x/\text{NiMoS}$, $\text{NiO}_x/\text{Ni}_3\text{S}_2$ (S) and $\text{MoO}_x/\text{MoS}_2$ (Mo). Reproduced with permission.^[89] Copyright 2020, Springer Nature. b) Schematic illustration for the synthesis process of $\text{R-CoC}_2\text{O}_4@\text{MXene}$.^[92] c) Differential charge density distributions of $\text{R-CoC}_2\text{O}_4@\text{MXene}$, the yellow and blue zones represent the charge accumulation or dispersion, respectively. Reproduced with permission.^[92] Copyright 2022, Springer Nature. d) Schematic illustration of HER at versatile active sites of MPIC.^[95] e) Water dissociation energy and f) ΔG_{H^*} of versatile active sites at MPIC. Reproduced with permission.^[95] Copyright 2022, American Chemical Society.

effect between MoS_2 and Ni_3S_2 but also providing a large number of active sites.^[90] Benefiting from this, a high current density of 1000 mA cm^{-2} was achieved with an overpotential of only 200 mV . Anchoring catalytically active species with excellent activity on conductive carriers to form heterostructures for synergistic HER catalysis is also a feasible strategy. Wang et al. ensured that Ni nanoparticles were firmly grown on MnO_2 nanowires by *in situ* exsolution. As a metal semiconductor, MoO_2 nanowires accelerate electron transfer, which further promotes the synergistic effect between Ni and MnO_2 heterostructures.^[91] Likewise, Peng et al. reported an interface-induced self-assembly strategy for the synthesis of hollow nanotube $\text{CoC}_2\text{O}_4@\text{MXene}$ precatalysts (Figure 7b).^[92] Thanks to the enhanced adsorbate accumulation and charge transfer of MXene, $\text{CoC}_2\text{O}_4@\text{MXene}$ underwent rapid reconfiguration ($\text{R-CoC}_2\text{O}_4@\text{MXene}$). The differential charge density indicates a significant electron redistribution behavior of $\text{R-CoC}_2\text{O}_4@\text{MXene}$ in a heterogeneous structure, which optimizes the adsorption energy of the reaction intermediates, thus delivering an excellent HER activity ($\eta_{1000} = 216 \text{ mV}$) (Figure 7c). Transition metal-based phosphides often have good HER activity. Combining multiple phosphides into a heterogeneous structure often has a one-plus-one effect. Ren's group reported an $\text{FeP}/\text{Ni}_2\text{P}$ heterostructured catalyst that requires an overpotential of only about 275 mV to achieve a current density of 1000 mA cm^{-2} in 1 M KOH .^[93] In another work, Cheng et al. synthesized a $\text{CoP}@\text{Ni}_2\text{P}$ electrocatalyst, which also possessed high performance with a current density of 500 mA cm^{-2} at a low overpotential of 209 mV .^[94] As reflected by DFT calculations, strong electronic interactions between Ni_2P and CoP optimize the HBE and improve the intrinsic activity. Moreover, the rich heterogeneous interface promotes electron transfer and provides more favorable active sites. Jian et al. developed a $1\text{T}_{0.63}\text{-MoSe}_2@\text{MoP}$ multiphase interfacial catalyst (MPIC), which possesses rich interface and a large number of defects.^[95] The construction of the multidirectional interface enhances the abundance of active sites and synergistically promotes the HER performance (Figure 7d–f). Consequently, $1\text{T}_{0.63}\text{-MoSe}_2@\text{MoP}$ displayed an outstanding HER activity with an overpotential of 358 mV to deliver 1000 mA cm^{-2} .

5.2. "Work with a Common Purpose": Interface Interaction to Create Active Sites

The previous design strategies have been used to optimize the adsorption–desorption capacity of the active site by adjusting the charge redistribution. In contrast, interfacial interaction refers to the mixing of the atomic orbitals of two interfaces when they combine. This coupled heterogeneous interface has the ability to activate the embedded sites and promote electronic conductivity, enabling the interface or its surrounding atoms to become a new active site.^[96–98] As an example, Liu et al. reported an $\text{NFCH}@\text{NiMoO}_4$ (NFCH-NMO) using molybdate modification in concert with carbonate hydroxide hydrate (NFCH) to construct atomic-level coupled heterostructures.^[99] The dual NS structure possesses abundant open channels at the high-energy phase interface, which enhances the kinetics induced by the modified electronic structure (Figure 8a). Explicitly, it only required an ultralow overpotential of 297 mV to reach a current density of

500 mA cm^{-2} . In another work, with an attempt to improve the kinetics of phosphate at high current densities, Qiao et al. introduced nickel hydro(oxy)oxide into Ni_2P to construct a strong electron-coupled interface.^[100] The differential charge density analysis showed that $\text{sc-Ni}_2\text{P}^{\delta-}/\text{NiHO}$ possessing a strong electron-coupled interface had more significant interfacial electron transfer relative to $\text{Ni}_2\text{P} + \text{NiHO}$ (Figure 8b), which facilitated the destabilization of water molecules in an alkaline solution. Similarly, Chen et al. filtered cobalt phosphide (Co_2P) and nickel phosphide (Ni_5P_4) with the lowest formation energy based on atomic calculations to construct heterogeneous interfaces for hydrogen adsorption.^[101] As shown in Figure 8c,d, the heterogeneous interface formed between the (303) facets of Ni_5P_4 and Co_2P optimizes and accelerates the adsorption process of hydrogen-containing intermediates. The corresponding adsorption-free energy with a $\Delta G_{\text{H}*}$ of -0.64 eV is closer to the ideal catalyst-free energy ($\Delta G_{\text{H}*} = 0 \text{ eV}$), so an ultralow overpotential of 267 mV at 1000 mA cm^{-2} was required.

Nitrogen-rich metal nitrides possess higher HER activity and corrosion resistance because of the influence of their abundant metal–N bonds on the charge distribution.^[102] However, nitride-rich nitrides are also more susceptible to the adsorption of excessive intermediates, which hinders catalytic activity at high current densities.^[103] Jiao et al. addressed this problem by constructing ultrathin heterojunctions of metal Co and nitride-rich nitrides ($\text{Co-Mo}_5\text{N}_6$) through a two-step hydrothermal-ammonia annealing process.^[104] The ultrathin NSs have abundant interstitial space and strong capillary forces. Meanwhile, the optimized electron redistribution at the interface between the N-rich phase and metal Co makes it easier for hydrogen adsorption at the $\text{Co-Mo}_5\text{N}_6$ interface, which enhances the H_2O adsorption energy and decreases the energetic barrier of H_2O dissociation. It only needs an overpotential of 280 mV to achieve an industrially meaningful current density (1000 mA cm^{-2}). In another work, Du et al. developed a facile anion-intercalation enhanced electrodeposition method for preparing a $\text{Co(OH)}_2\text{-CeO}_2$ precursor, which was then nitridated selectively to obtain $\text{Co}_4\text{N}-\text{CeO}_2$ NS arrays.^[105] Notably, it achieved an excellent HER activity of 500 mA cm^{-2} at a low overpotential of 190 mV . Based on the parallel alignment of the lattice stripes on the (111) plane of Co_4N and the (111) plane of CeO_2 in high-resolution transmission electron microscope (HRTEM), it was able to observe the obvious interface formed between them (Figure 8e,f). Due to this interface, the water dissociation energy barrier decreased to 0.74 eV compared to the Co_4N (111) surface (1.74 eV), and the HBE was regulated to be a more thermo-neutral value, which was the reason for the excellent activity of $\text{Co}_4\text{N}-\text{CeO}_2$.

As a noble metal, Ru is relatively inexpensive compared with other precious metals (e.g., Pt, Ir, and Rh), so it has promising prospects in HER.^[106] Nevertheless, Ru-based nanomaterials still suffer from relatively high overpotential and poor stability.^[107,108] The combination of other materials with Ru to build heterogeneous interfacial structures with enhanced electron transfer not only optimizes the catalytic performance of HER but also achieves excellent catalytic stability. Yang's group has demonstrated that a $\text{RuO}_2\text{-NiO}$ heterogeneous structure with a hybrid interface can effectively modulate the electrical conductivity to achieve lower electrochemical impedance.^[109] Moreover, the accumulation of electrons at the Ru site at the interface weakens the H adsorption on O sites. In addition, Li et al. combined

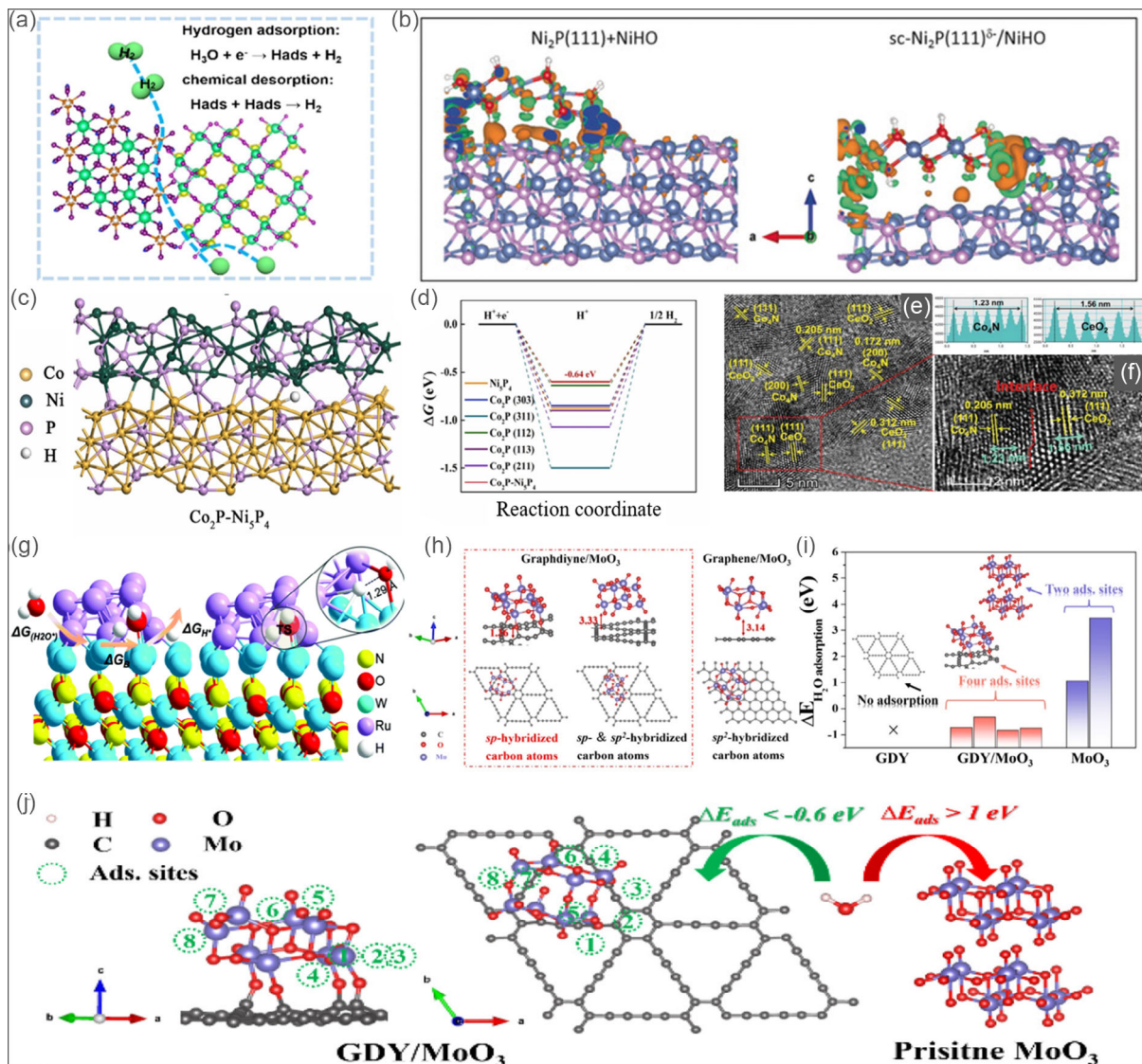


Figure 8. a) Schematic illustration of the HER catalytic mechanism of NFCH-NMO. Reproduced with permission.^[99] Copyright 2022, Elsevier. b) Differential charge density distributions of Ni₂P(111)+NiHO and sc-Ni₂P(111)^{δ+}/NiHO. Green and orange contours represent electron accumulation and depletion, respectively. Reproduced with permission.^[100] Copyright 2019, Wiley-VCH GmbH. c) Theoretical calculation model of Ni₅P₄-Co₂P for hydrogen adsorption.^[101] d) ΔG_{H^*} of Different crystal planes of Co₂P, Ni₅P₄, and the interface of Ni₅P₄-Co₂P. Reproduced with permission.^[101] Copyright 2022, Elsevier. e,f) HR-TEM images for the Co₃N-CeO₂. Reproduced with permission.^[105] Copyright 2020, Wiley-VCH GmbH. g) Schematic illustration of the reaction mechanism of Ru/WNO@C. Reproduced with permission.^[110] Copyright 2019, RSC Publishing h) Theoretical model construction of MnO₃ in different positions of GDY and graphene.^[113] i) calculated H₂O adsorption energy on GDY, MoO₃, and GDY-MoO₃.^[113] j) Adsorption sites of H₂O on GDY/MoO₃ and schematic illustration of H₂O adsorption on pristine MoO₃ and GDY/MoO₃. Reproduced with permission.^[113] Copyright 2021, American Chemical Society.

experiments and theoretical calculations to propose that the Ru/WNO interface becomes the main active center when Ru nanoclusters are anchored to W_{0.62}(N_{0.62}O_{0.38}) (WNO) nanowires.^[110] The apparent electron enrichment at the interface promotes the dissociation energy barrier and adsorption energy barrier during the HER process (Figure 8g). Meanwhile, Ru/WNO with low Ru loading is in demand for industrial applications, which possesses an excellent mass activity of 4095.6 mA mg⁻¹ with an overpotential of only 50 mV. Recently, Li et al. similarly exploited charge redistribution at the interface between Ru clusters and layered

oxide perovskite Sr₂RuO₄ to achieve efficient HER activity (1000 mA cm⁻² with the overpotential of 278 mV).^[111]

When the two components are at similar energy levels, their atomic orbitals can also form trans-interfacial chemical bonds, which can trigger faster electron transfer between the interfaces.^[112] As shown in Figure 8h,i, a simulation of the interfacial sp hybridization between graphitic diyne and molybdenum oxide is constructed, which reveals that the hybridization is constituted in the form of interfacial C—O—Mo bonds that have more adsorption (ads) sites.^[113] Based on the previous, GDY/MoO₃ was

synthesized on 3D copper foam by Guo et al.^[113] After the addition of MoO₃, significant redshifts in the G-band and conjugated diyne links modes ($-C \equiv C-C \equiv C-$) could be observed on the Raman spectra; meanwhile, the “A-peak” of the aromatic carbon–carbon bond in the six-membered carbon ring symbolized by XANES spectra was shifted to a lower energy position. All of these results indicated the formation of sp-hybridized C—O—Mo bonds at the GDY/MoO₃ interface. As the interfacial “sp C—O—Mo hybridization” promotes the transfer of electrons from GDY to MoO₃, it creates abundant oxygen vacancies on MoO₃ and provides more active sites at the interface suitable for H₂O adsorption (Figure 8j).

5.3. “Each Performs Its Own Functions”: Creating Dual Active Sites to Optimize Reaction Pathways

As mentioned in the previous section, HER under alkaline conditions is often affected by more factors than the hydrogen adsorption capacity and is also limited by the initial water dissociation. Although the methods mentioned earlier that are used to modulate the electronic structure of the catalysts are able to solve both hydrogen adsorption and water dissociation energy barriers, the synthesized materials usually have many uncertainties.^[114] An alternative strategy is to construct dual active site catalysts that combine the adsorption capacities of different intermediates at different sites, which is certainly another catalyst design strategy of interest.

In addition to regulating the electronic structure, defective sites can also act as active sites to synergistically enhance the catalytic activity of HER. Yang et al. proposed an electrochemical activation to stimulate the formation of defective FeOOH on the Cu–Fe₃O₄ catalyst surface.^[115] The significant enhancement of oxygen vacancy signal determined by the electron paramagnetic resonance and the variation of the wavelet transforms for the k^2 -weighted Cu K-edge extended X-ray absorption fine structure (EXAFS) curves indicated peaks of Cu—O and Cu—Cu/Fe bonds that were broader than those of a Cu–Fe₃O₄ precursor, which proves the presence of a large number of oxygen vacancies in Cu–FeOOH/Fe₃O₄. Based on a large number of experiments, the 2D charge difference isosurface and DFT calculation simulations were analyzed (Figure 9a). The corresponding results indicate that electrons accumulate around oxygen vacancies and rearrange at the interface of the Cu–FeOOH/Fe₃O₄, which can effectively reduce the energy barriers for H₂O dissociation and hydrogen generation. Figure 9b demonstrates the synergistic hydrogen precipitation mechanism of Fe and O sites, which efficiently improves the HER performance of the catalyst (1000 mA cm⁻² at an overpotential of about 350 mV).

The doping of the second active site is another strategy to achieve the previous idea. Liu’s group designed a Ni–W bimetallic catalyst prepared by a rapid dehydration method of W-doped Ni(OH)₂, which achieves efficient HER activity ($\eta_{500} = 309$ mV).^[116] The electron migration between Ni and W resulted in more empty d orbitals on the W site for adsorption of H₂O, which was dissociated into H* and OH⁻, while the surrounding Ni sites were able to adsorb the H*. As another adsorbed water molecule dissociated at the W site, the new H* combined with Ni-H via a Heyrovský step to generate H₂. Phosphorus (P), which is often used for

doping with transition metals due to its weak electronegativity, can be used as an active site and exhibits unexpected HER catalytic behaviors. Chai et al. revealed that P-doped inverse spinel Fe₃O₄ (P-Fe₃O₄) has an unusual HER catalytic mechanism: 1) Fe_{oct} and O_{lat} in Fe₃O₄ enable water molecules to adsorb as dimers (hydrogen-bonded linkages) on the surface to form a unique eight-membered ring structure, and this achieves a unique bimolecular Volmer reaction mechanism that lowers the water dissociation energy barrier; 2) P doping provides adsorption sites with ΔG_{H^*} close to zero ($\Delta G_{H^*} = 0.012$ eV), solving the lack of inherent hydrogen absorption active sites in Fe₃O₄ (Figure 9c).^[117] Therefore, P-Fe₃O₄ exhibits a unique catalytic mechanism due to the synergistic effect of Fe₃O₄ and P double site (Figure 9d). Noteworthy, a very large cathodic current density of 1000 mA cm⁻² can be generated at $\eta \approx 247$ mV. Similarly, Chen et al. synthesized P and B codoped Co–B–P NS arrays by a one-step chemical deposition method, and the resultant electrocatalyst also achieved high current densities of 1000 and 2000 mA cm⁻² at overpotentials as low as 165 and 220 mV.^[118] As shown in Figure 9e, due to the difference in electronegativity between P and B, the production of partially positively charged Co (Co^{δ+}) is promoted. In the Volmer step, the undercoordinated Co^{δ+} and the dangling P (P^{δ-}) interact with O and H in H₂O, respectively, which enhances the adsorption of H₂O and weakens the HO–H bond of the adsorbed H₂O, thus promoting the dissociation of water. Then, the Heyrovský step occurs for the co-adsorption of H* by the adjacent P and Co sites. Ru element has the strongest water dissociation ability among all noble metals, but its relatively negative ΔG_{H^*} tends to limit its performance in basic HER. The doping of Ru with other catalysts with excellent H* adsorption energy barriers to construct two-site catalysts can effectively solve the previous problems. Based on this property, Tong’s group accomplished the doping of Ru elements on Ni₂P/NiO heterostructured layered flower-like NSs (Ru-Ni₂P/NiO/NF).^[119] The coupling effect of the Ni₂P/NiO heterostructure can effectively promote H* adsorption ($\Delta G_{H^*} = -0.06$ eV), which synergistically promotes the electrocatalytic HER activity with the strong H₂O adsorption energy of the Ru site.

Another approach is to build dual active sites using a heterogeneous structure. Huang et al. have proposed that the electronic state of active Ni₃N is regulated by using 2M–MoS₂ as an electron reservoir (Figure 9f).^[120] Mo K-edge EXAFS spectra reveal a periodic decrease in the oscillation curve of Ni₃N@2M–MoS₂, and the HRTEM image shows significantly interacting crystal surfaces, both indicating the formation of Ni₃N@2M–MoS₂ heterostructures (Figure 9g–i). The Ni sites in Ni₃N@2M–MoS₂ with hybridized interfaces exhibit a low hydrolysis energy barrier (0.653 eV), while the N sites have suitable free energy for hydrogen adsorption. The synergistic effect of the different sites greatly contributes to the overall HER kinetic, satisfying the requirement for industrially robust water electrolysis. Similarly, Fan et al. reported a Ni₂P/WO_{2.83} heterogeneous interfacial microsphere electrocatalyst with a large number of oxygen defects loaded on nickel foam.^[121] Among that, WO_{2.83} can effectively facilitate H₂O dissociation, and Ni₂P can easily accelerate the conjoined desorption of H*, thereby driving a large current density of 1000 mA cm⁻² and a relatively low overpotential of 254.5 mV. Likewise, Liu et al. constructed large-scale WP–W₂C heterostructures with nanoporous structures that synergistically improved

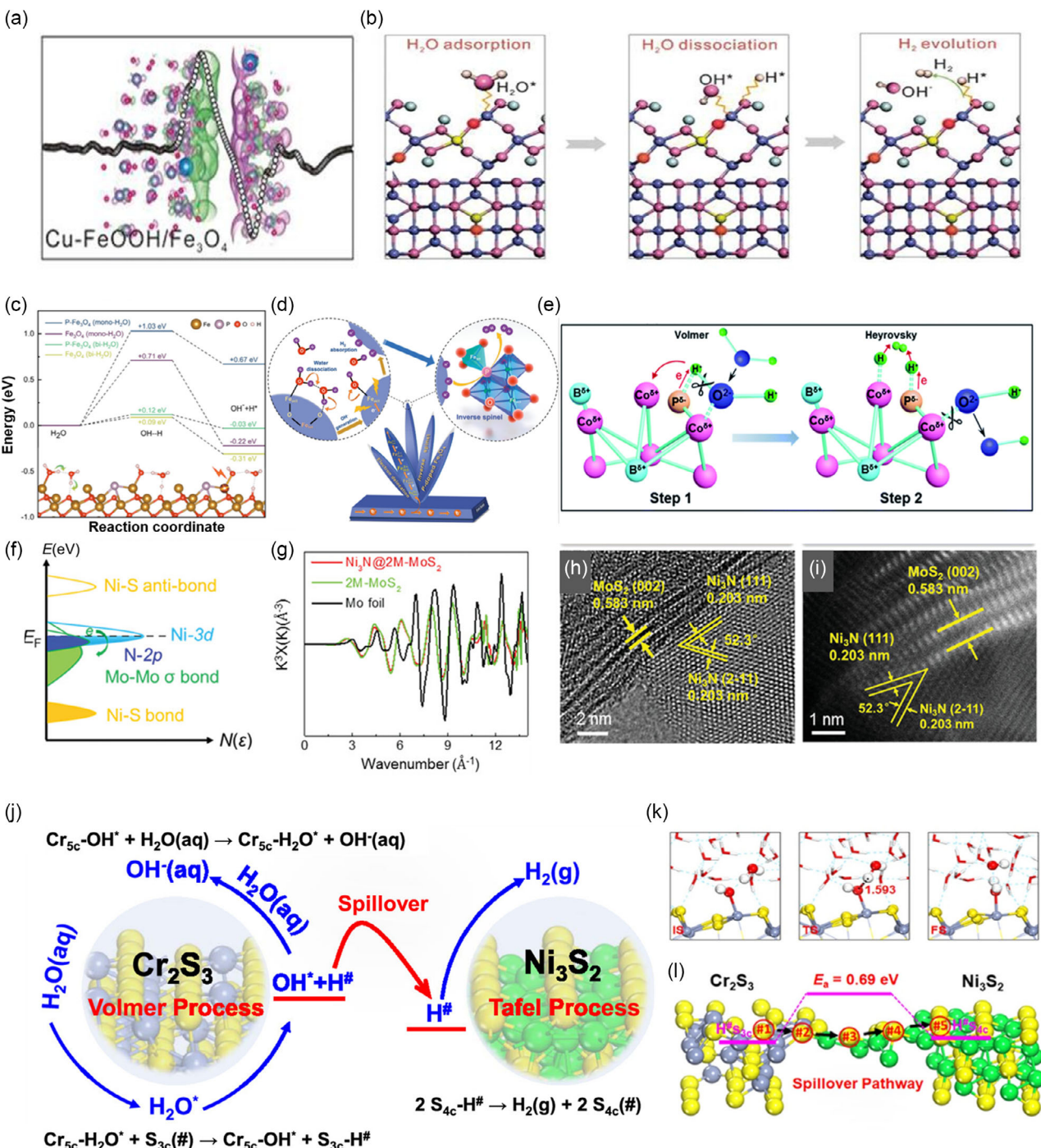


Figure 9. a) The charge density distribution and b) Schematic diagram for the HER reaction pathway on Cu–FeOOH/Fe₃O₄. Reproduced with permission.^[115] Copyright 2022, Wiley-VCH GmbH. c) The unique H₂O adsorption-dissociation mechanism of P–Fe₃O₄ and the corresponding kinetic energy barrier for water dissociation.^[117] d) Schematic illustration of the HER catalytic mechanism of P–Fe₃O₄. Reproduced with permission.^[117] Copyright 2021, Wiley-VCH GmbH. e) Schematic illustration of the HER catalytic mechanism of Co–B–P/NF. Reproduced with permission.^[118] Copyright 2018, The Royal Society of Chemistry. f) Schematic illustration of the electronic state regulation mechanism of 2M–MoS₂ as an electron reservoir.^[120] g) Mo K-edge EXAFS oscillations.^[120] h) HRTEM and i) HAADF-STEM images of Ni₃N@2M–MoS₂. Reproduced with permission.^[120] Copyright 2022, Wiley-VCH GmbH. j) Schematic illustration of the reaction mechanism of Ni₃S₂/Cr₂S₃@NF two-site synergistic effect.^[16] k) Water dissociation process under (i) conventional environment or (ii) water-logged environment.^[16] l) Hydrogen spillover route of Cr₂S₃/Ni₃S₂. Reproduced with permission.^[16] Copyright 2022, American Chemical Society.

electrocatalytic activity and stability at high current densities under alkaline conditions.^[122] The tight connection between the W substrate and WP-W₂C reduced the electrode resistance and ensured the efficiency of electron transport during HER. More importantly, the charge redistribution at the WP-W₂C interface ensured a low water dissociation energy barrier of 0.20 eV, much lower than that of W₂C (0.44 eV) and WP (0.23 eV). Moreover, the P sites at the interface exhibited an appropriate Gibbs free energy for H adsorption with an ΔG_{H^*} of 0.17 eV. Thus, with the synergistic effect of the dual sites at the interface, the HER performance of the WP-W₂C catalyst is superior to that of the commercial Pt/C catalyst, reaching 1000 mA cm⁻² with an overpotential of 560 mV. In another work, Fe@Fe_xNiO/Ni@Ni_yCoP also achieved excellent HER performance through a similar synergistic two-site interaction, it could display a large current density of 1500 mA cm⁻² with an overpotential of 129 mV.^[123] Recently, we demonstrated the use of the hybridization design idea to create coherent synergistic effects with Ni₃S₂/Cr₂S₃ nanoparticles grown directly on nickel foam, which provides new mechanistic insights to achieve ampere-scale current density operation.^[16] The strong adsorption of H₂O and desorption of OH⁻ at the Cr_{5C} site of Cr₂S₃ can be achieved through a heterolytic cleavage process and a new water-assisted desorption mechanism, respectively (Figure 9j). Notably, we consider the effect of high hydrogen coverage at high current densities on the inhibition of the active site. In combination with experimental and theoretical data, such as the systematically microkinetic analyses by the CATKINAS code and kinetic isotope effect experiments, we determined that the Ni₃S₂/Cr₂S₃ hybridization interface bridges the H[#] hydrogen spillover from the hydrogen-rich site (Cr₂S₃) to the H-deficient site (Ni₃S₄) (Figure 9k,l). As a result, ampere-level current densities can be achieved at ultra-low overpotentials (for $j = 1, 2, 3$, and 3.5 A cm⁻², $\eta_j = 227, 240, 246$, and 251 mV).

The above describes three commonly used strategies (optimization of active site's electronic structure, construction of active interfaces, construction of dual active sites) to enhance the intrinsic activity of HER catalysts, in fact, they are not isolated from each other, but complementary to each other. The use of the previous strategies in a balanced manner is beneficial to further enhance catalyst activity. For example, the efficient activity and stability at a current density of 1000 mA cm⁻² were recently achieved by Li et al. using the in situ formation of Ru clusters from the layered oxide chalcogenide Sr₂RuO₄ (SRO).^[111] Experimental and DFT calculations showed that charge redistribution occurred at the interface between the native SRO and Ru clusters, which weakened the hydrogen adsorption capacity of the Ru active sites through interfacial interactions, ultimately leading to high intrinsic HER efficiency.^[111] Similarly, Mu et al. used doping to modulate the electronic structure of the Ru active site at the atom-scale symmetry-breaking interfaces, which achieved excellent HER performance at the amperometric level.^[124] In addition to this, Feng et al. exploited the electronic synergy between Ru nanoparticles (Ru-NP) and single atoms (Ru-SA) to optimize the electronic structure of both active sites while constructing a dual active site.^[125] It makes Ru-NP the main contributor to the kinetic water dissociation process, while Ru-SA mainly promotes the formation of hydrogen. It achieves an excellent performance of 1000 mA cm⁻² with an overpotential of only 251 mV.^[125]

6. Macroscopic Design of Electrodes

In addition to the modulation of intrinsic activity, fast mass transfer diffusion processes and excellent mechanical and structural stability are also crucial for electrocatalysts applied in industrial electrolytic conditions with high current densities. After understanding electrocatalyst design and activation strategies, we will next overview the macrostructural fabrication of the electrodes to enhance the mass transfer and mechanical stability of the electrode. Table 3 summarizes all the excellent catalyst properties in this section.

6.1. Self-Supported Electrocatalysts

Most HER catalysts in the laboratory research stage are powdered metal-based catalysts with nanostructures. Typically, the powder catalysts need to be coated on the collector (electrode substrates) by polymeric binders. This approach inevitably increases the electrode resistance and inhibits the mass transfer capability of the materials. At the same time, the powder catalysts tend to fall off from the collector by simple mechanical attachment during long-term high current density HER catalysis, which greatly affects their long-term stability under industrial conditions. In contrast, self-supported electrocatalysts directly grown on the surface of the collector during the electrode preparation process without the use of a binder can solve the previous problems well. This approach also reduces the complicated coating steps and the use of expensive polymer binders, thus reducing the manufacturing cost and time. Therefore, self-supported electrocatalysts should be more suitable for industrial-scale applications.

Water/solvent thermal synthesis is one of the most common methods for the preparation of self-supported electrodes. Generally, the nanocatalysts are nucleated on the substrate surface by applying a certain temperature and pressure in a closed system to form a self-supporting electrode with high stability. For instance, Yin et al. in situ prepared an FeIr alloy grown on the surface of nickel foam using a hydrothermal method, which possesses a unique volcano-like morphology.^[126] The unique volcano-like structure of FeIr alloy provided a larger specific surface area for the electrode, which greatly promotes HER activity. Moreover, the self-supported structure can maintain a long-term stability, showing almost no decay for 124 h at -1000 mA cm⁻². Moreover, by changing various conditions, such as the reaction time and precursor concentration of the solvothermal reaction, the morphology of the self-supported electrode can be tuned to achieve better performance.^[127,128] For example, Zou's group used a simple solvothermal reaction to synthesize ultrathin NS-based hollow MoO_x/Ni₃S₂ composite microsphere catalysts on nickel foam by controlling different reaction conditions (e.g., reaction time, structure-directing agent concentration, etc.), further enhancing HER catalytic performance.^[127]

Although solvothermal reactions can modulate the catalyst morphology in several ways, there are still many limitations on catalyst types. Therefore, a posttreatment process is often required after the hydrothermal reaction. Annealing heat treatment is a common treatment, such as phosphorization,^[71,74,75,94] nitrogenization,^[78] sulfidization,^[76,80] reduction,^[85,91] etc. Feng et al. used hydrothermal reaction to presynthesize NiMoO₄ on

Table 3. Representative HER electrocatalysts through the macroscopic design of electrodes.

Strategy	Catalyst ^[ref.]	Electrolyte	Overpotential (mV@500 mA cm ⁻²)	Overpotential (mV@1000 mA cm ⁻²)	Stability
Self-supported electrocatalysts	FeIr/NF ^[126]	1 M KOH	246	327 (1000 mA cm ⁻²) 461 (2000 mA cm ⁻²)	1000 mA cm ⁻² for 120 h
	MoO _x /Ni ₃ S ₂ /NF ^[127]	1 M KOH	486	/	≈15 mA cm ⁻² for 200 h
	MoNi ₄ ^[129]	1 M KOH	≈70 (600 mA cm ⁻²)	/	200 mA cm ⁻² for 10 h
	D-NiO-Pt ^[133]	1 M KOH	407	/	10 mA cm ⁻² for 100 h
	Co-P ^[140]	1 M KOH	/	290	1000 mA cm ⁻² for 3000 h
	Ni-Co-P/CFP ^[136]	1 M KOH	170	295	1000 mA cm ⁻² for 300 h
	CoMoS _x /NF ^[87]	1 M KOH	269	/	500 mA cm ⁻² for 100 h
	PS-Cu ^[146]	1 M KOH	/	1200 (1200 mA cm ⁻²)	100 mA cm ⁻² for 30 h
Design of electrode surface	CuMo ₆ S ₈ /Cu ^[147]	1 M KOH	/	320 (1000 mA cm ⁻²) 334 (2500 mA cm ⁻²)	2500 mA cm ⁻² for 100 h
	Co(OH) _x @NiMoO _x @NF ^[151]	1 M KOH	185	322	1000 mA cm ⁻² for 11 days
	Ni ₂ P-CoOOH ^[150]	1 M KOH	≈160	≈400 (2000 mA cm ⁻²)	≈1800 mA cm ⁻² for 100 h
	MoS ₂ /Mo ₂ C ^[50]	1 M KOH	191	220	200 mA cm ⁻² for 20 h
	Pt/Ni-Mo ^[161]	1 M KOH	/	33 (1000 mA cm ⁻²) 42 (2000 mA cm ⁻²)	2000 mA cm ⁻² for 140 h
		1 M KOH + 0.5 M NaCl	/	113 (2000 mA cm ⁻²)	500 mA cm ⁻² for 24 h
		6 M KOH	/	/	500 mA cm ⁻² for 24 h
	Ni ₂ P/NF ^[159]	1 M KOH	/	306 (1000 mA cm ⁻²) 368 (1500 mA cm ⁻²)	-0.240 to -0.65 V for 24 h
Development of new substrates	C-Ni _{1-x} O/3DPNi ^[171]	1 M KOH	≈210	245	2.2 V (≈800 mA cm ⁻²) for 16 h (1 M KOH, 80 °C)
	3DPM NiMoAS ^[168]	1 M KOH seawater	282	/	500 mA cm ⁻² for 120 h
	Ni-P-B/paper ^[173]	1 M KOH	251	276	1000 mA cm ⁻² for 240 h
	MoNi ₄ /SSW ^[172]	5 M KOH, 70 °C	161	/	150 mA cm ⁻² for 150 h

the surface of nickel foam, which was later annealed in an H₂/Ar atmosphere to obtain MoNi₄ nanoparticles on the surface of MoO₂ rectangles (MoNi₄/MoO₂@Ni).^[129] Compared with pure NiMoO₄ before annealing, MoNi₄/MoO₂@Ni exhibited superb alkaline HER activity ($\eta_{600} = 70$ mV). In addition, the posttreatment of materials using plasma technology has gradually received much attention in recent years.^[89,130–133] This method is a simple, clean, efficient, and scalable strategy. For example, Qi et al. constructed defect-anchored Pt atoms in NiO NSs hydrothermally grown on carbon paper using Ar plasma to create Pt single-atom catalysts with high stability.^[133] Besides, Hou et al. used oxygen plasma treatment to obtain NiMoO_x/NiMoS heterostructure arrays, which exhibit excellent durability for 300 h (Figure 10a).^[89] Although the solvothermal method is adequately used at the laboratory stage, the size of the autoclave and the high-temperature and high-pressure environment will still restrict the practical electrode area, which hinders its commercially scalable application.

Electrochemical deposition is another suitable synthesis method for self-supported electrodes. Electrochemical deposition is simple and efficient with short reaction times compared to the high-temperature limitations of solvothermal reactions, and the catalyst loading and catalyst morphology can be improved by

controlling the deposition time. The commercial electrode preparation process, Watts plating, is one of the electrochemical deposition processes.^[134,135] There are many self-supporting electrodes prepared by electrodeposition that meet industrially high current densities and have demonstrated exceptional stability.^[136–140] For instance, Liu et al. prepared porous cobalt phosphide by electrochemical anodization of commercially available cobalt foam followed by phosphorylation.^[140] Correspondingly, it could stably operate for at least 3000 h at a constant current density of 1000 mA cm⁻² and a voltage of 0.290 V versus RHE. In another work, Zhang et al. exploited a novel layer-exfoliated layered Ni-Co-P catalyst by electrode cyclic voltammetry electrodeposition.^[136] Due to the unique structure of the layered catalyst, the inner catalyst layer was re-exposed to continue working after the outer layer of the catalyst was peeled off, ensuring the durability of catalytic activity. Notably, it can maintain at least 300 h at an extremely high current density of 1000 mA cm⁻². However, there are still some problems that need to be solved in the electrodeposition method, such as uneven deposition areas and a low utilization ratio of the electroplating solution, which will increase cost.

Wet chemical methods have also gained a lot of attention in the preparation of self-supported electrodes. Like electrodeposition methods, wet chemical methods require mild reaction

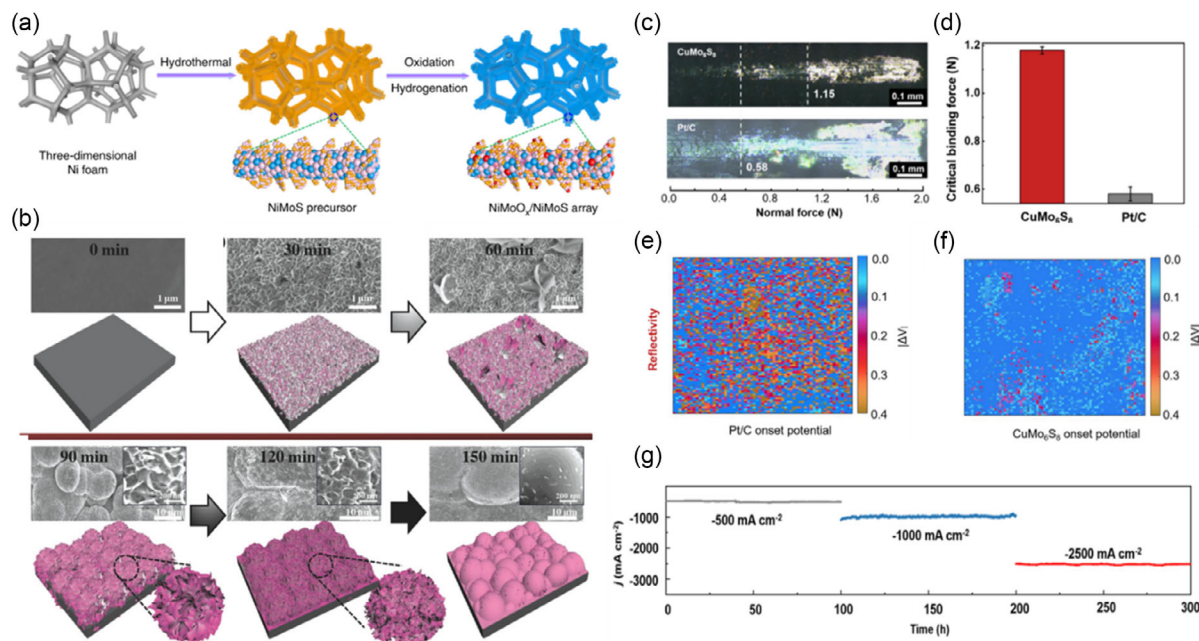


Figure 10. a) Synthesis illustration of NiMoO_x/NiMoS array. Reproduced with permission.^[89] Copyright 2020, Springer Nature. b) Schematic illustration and SEM images of the reaction time regulated morphology. Reproduced with permission.^[147] Copyright 2018, Wiley-VCH GmbH. c) Digital photo of microscratches. The dashed line represents the critical force value of the catalyst.^[147] d) Statistics on the critical adhesion forces of CuMo₆S₈ and Pt/C.^[147] e,f) Mappings of difference values of onset potentials of the Pt/C and CuMo₆S₈/Cu electrodes.^[147] g) HER stability curves of CuMo₆S₈/Cu. Reproduced with permission.^[147] Copyright 2022, Springer Nature.

conditions and a controlled operating procedure.^[87,128] For example, Jiang et al. in situ grew Chalcogels (CoMoS_x/NF) on nickel foam substrates by coprecipitation of Co²⁺ and [MoS₄]²⁻ under environmental conditions. The resultant abundance of defects during the coprecipitation process significantly enhances its catalytic activity.^[87] The electroplating method is another wet chemical method. Traditional heat treatment reactions such as phosphorization or boronization usually require high temperature to break down the phosphate, which not only consumes time and resources but also brings some safety risks. Electroless plating (EP) enables phosphorization or boronization to be performed directly on various substrates.^[141–143] Take the work of Guo et al. as an example, they used dimethyl ammonium borane (DMAB, Et₂NHBH₃) as a reducing agent and submerged various substrates in an aqueous EP bath with CoSO₄ for several minutes to obtain novel and robust boride based electrodes.^[141] The catalyst morphology can be modified by regulating the impregnation time (Figure 10b).

In addition to the previous commonly used methods for preparing self-supporting electrodes, it is worthwhile to develop unique methods to prepare electrodes for further research and discussion. PS is often used for the preparation of industrial Raney nickel electrodes.^[144,145] Du et al. utilized this process to spray Cu powder onto copper plates as HER electrodes (PS–Cu) under high-velocity airflow.^[146] The geometric phase analysis result reveals that tensile strain was retained in the PS–Cu samples, which enhances the intrinsic activity of the catalyst and promotes porous structure stabilization. A simple thermal treatment is another method that can be used to achieve industrial scale.^[110,147–149] Liu et al. prepared a

Chevrel-phased CuMo₆S₈ grown on Cu foam (CuMo₆S₈/Cu) using a simple grinding-heat treatment process.^[147] The CuMo₆S₈/Cu electrode displayed a robust electrocatalyst-support interface binding strength, with a critical binding force that was almost double that of the Pt/C electrode (Figure 10c,d). Notably, they quantified the extent of electrocatalyst exfoliation using an in-situ total internal reflection imaging characterization method, strongly confirming the mechanical stability of CuMo₆S₈/Cu. As shown in Figure 10e,f, the area of small difference values of over 0.05 V almost disappears on CuMo₆S₈ but easily appears on Pt/C. The magnitude of the difference represents the degree of electrocatalyst stripping, which indicates that CuMo₆S₈ has much better mechanical stability than Pt/C. Impressively, CuMo₆S₈/Cu remains stable for more than 100 h at a very high current density of 2500 mA cm⁻² with a low overpotential of 334 mV (Figure 10 g).

6.2. Modification of Electrode Surface

Modifying the macrostructure of the catalyst on the electrode, for instance, the structure of the multidimensional catalytic surface can effectively expose more active sites per unit mass to improve HER performance.^[44,150–153] Moreover, the multidimensional structure implies a closer interface between the electrode and the electrolyte, which shortens the ion diffusion path and facilitates the release of bubbles.^[154,155] Recently, our group designed a multidimensionally hierarchical structure with 1D Co(OH)_x NSs growing on 2D NiMoO_x nanorods.^[151] The nanorods enhance the electrochemically active surface area of the electrode, while the 2D Co(OH)_x NSs attached to NiMoO_x nanorods

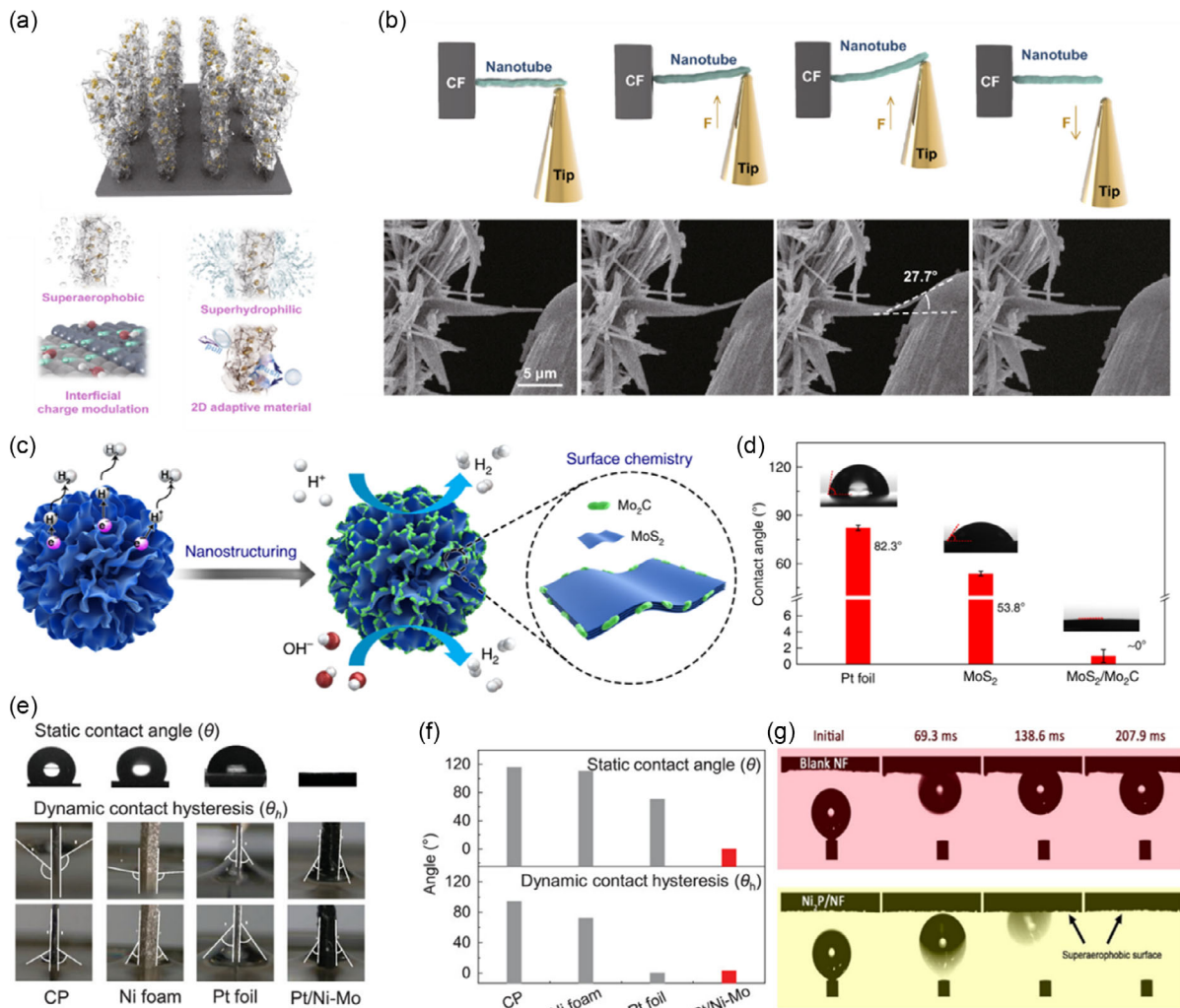


Figure 11. a) Catalytic structural model and structural advantages of Ni₂P-CoOOH.^[150] b) In situ bending restoration measurements by SEM probe. Reproduced with permission.^[150] Copyright 2020, Springer Nature. c) Schematic illustration of the structure of MoS₂/Mo₂C.^[50] d) Contact angle test on the surface of Pt foil, MoS₂, MoS₂/Mo₂C with 1 M KOH. Reproduced with permission.^[50] Copyright 2019, Springer Nature. e) the static contact angles and dynamic contact angle hysteresis on the surface of different catalysts.^[161] f) Statistical graph of contact angle values. Reproduced with permission.^[161] Copyright 2021, Wiley-VCH GmbH. g) Digital image of the dynamic hydrogen bubble adsorption process on the surface of Ni₂P/NF and blank NF. Reproduced with permission.^[159] Copyright 2019, American Chemical Society.

accelerate the mass transfer effect from the electrode to the electrolyte due to the heterogeneous interface between the two components. Surprisingly, Co(OH)_x@NiMoO_x@NF remained stable at 1000 mA cm⁻² for 11 days with no visible decay ($\eta_{1000} = 332$ mV). In addition, the 2D CoOOH flakes encapsulating Ni₂P into tubular arrays synthesized by Zhai et al. also showed great potential for industrial electrolytic water applications. The effect of multiscale structural modulation allows Ni₂P-CoOOH to exhibit extraordinary advantages in both mass transport and structural stability (Figure 11a).^[150] Impressively, they performed multiple bend-restoration tests on the material using SEM probes (Figures 11b,c). After testing, the material was able to recover to its initial state, indicating that the interweaving of nanotubes and stacked interlaced NSs endowed the nanotubes with high torsional resistance and high fatigue

strength, which is one of the reasons why Ni₂P-CoOOH can maintain stability for over 100 h at fixed current densities of 1800 mA cm⁻².

The increased electrochemically active surface area also leads to active bubble generation and coverage, so it is also crucial to accelerate the bubble detachment from the electrode surface.^[156] Wettability design of the electrode surface is a common strategy to solve the previous problem. Since the HER occurs at the three-phase interface, both the bubble contact angle (θ_b) and the water contact angle (θ_w) play a key influence on the reaction mass transfer.^[157,158] Various studies have shown that the construction of superanaerobic ($\theta_b > 150^\circ$) or superhydrophilic ($\theta_w < 5^\circ$) electrode surfaces facilitate mass transfer at high current densities.^[157] The excellent hydrophilicity of the electrode enables the electrolyte to fully contact the active sites, which reduces

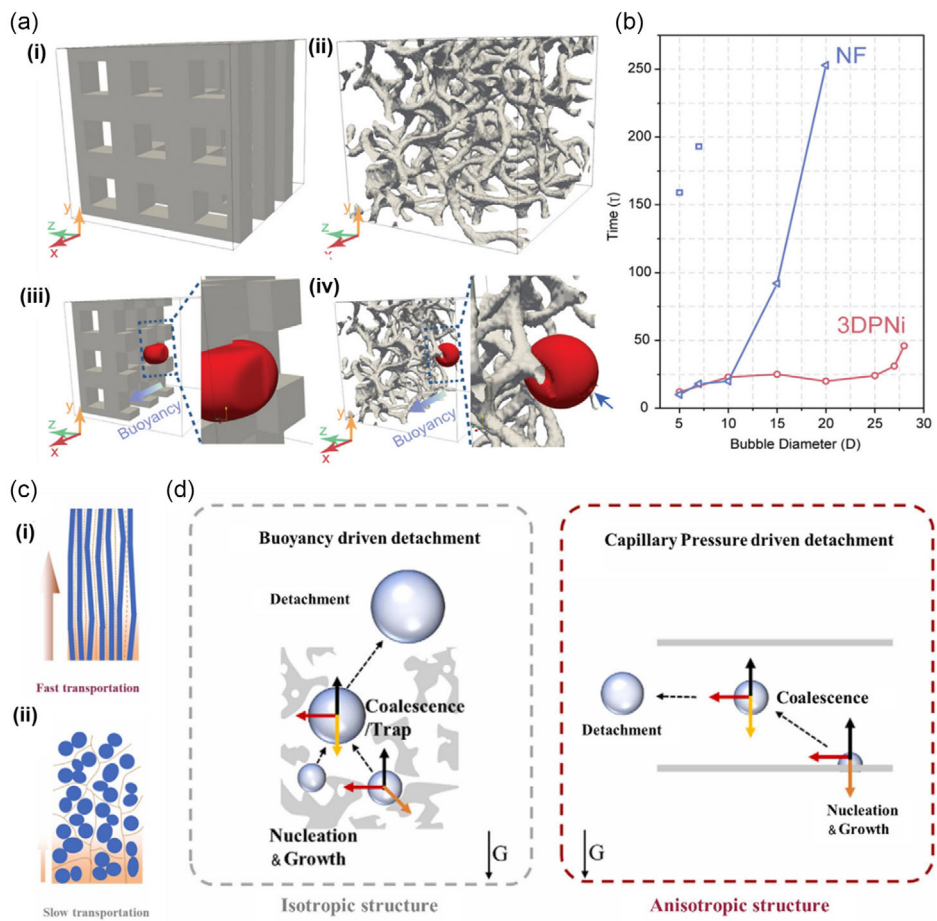


Figure 12. a) Structure model of (i) 3DPNi and (ii) NF; and bubble deformation on (iii) 3DPNi and (iv) NF during bubble transport.^[171] b) Comparison of bubble detachment time between 3DPNi and NF. Reproduced with permission.^[171] Copyright 2020, Wiley-VCH GmbH. c) liquid transfer path in (i) 3DP NiMoAS and (ii) 3DP NiMoS.^[168] d) Bubble transfer pathways in 3DP NiMoAS and 3DP NiMoS electrodes. Reproduced with permission.^[168] Copyright 2022, Elsevier.

the interfacial ohmic resistance; the superanaerobic property realizes the rapid detachment of H₂ produced after HER reaction, which prevents the bubble aggregation from disturbing the mechanical stability of the catalyst and also rapidly liberates the active sites for efficient catalytic processes.^[159–164] As shown in Figure 11d, Liu et al. synthesized MoS₂/Mo₂C nanomicrospheres with micron-scale and nanoscale roughness.^[50] The electrolyte contact angle of MoS₂/Mo₂C is almost 0°, indicating its superhydrophilic property. Meanwhile, the hydrogen bubbles on MoS₂/Mo₂C rapidly detach from the electrode surface at a size of less than 0.2 mm only due to the strong capillary force generated by the rough surface. Due to the electrode's increased mass transfer kinetics at high current densities, there is a significant increase in catalytic activity. The dynamic electrolyte contact angle test is closer to the actual situation during HER catalysis. Liu et al. measured the dynamic contact hysteresis angle (θ_h) using the Wilhelmy equilibrium method (Figure 11e,f).^[161] They have synthesized Pt/Ni-Mo with a static contact angle close to 0° and a dynamic hysteresis contact angle of only 3°, which further demonstrated that a good mass transfer process could occur between the electrolyte and electrode. Meanwhile, the superanaerobic structure is also

promising to achieve high current HER.^[159,165] As shown in Figure 11g, the blank foam Ni surface is prone to bubble retention, while the Ni₂P/NF surface prepared by Yu et al. can rapidly promote the detachment of H₂ bubbles. Therefore, Ni₂P/NF exhibits efficient electrocatalytic activity and stability.^[159]

6.3. Development of New Substrates

Metal foams (e.g., nickel foam, copper foam, etc.) are commonly used as electrode substrates in the laboratory development stage because they have a unique porous structure that enhances a larger area for catalyst growth, and they possess excellent electrical conductivity. However, since industrial flow-through electrolyzers often require the electrodes to be assembled, the foam structure may be damaged during this process, which in turn leads to a series of issues, including catalyst shedding. By contrast, porous nickel mesh is often used as the electrode substrate in practical applications, which sacrifices a large amount of electrode area as a cost. Therefore, the development of some novel electrode substrates has great potential for both scientific and industrial applications.

3D printing technology has advanced rapidly in recent years, and it has excellent operability in creating unique and ordered microscopic chemical structures.^[166–169] This is an effective way to solve the bubble mass transfer problem.^[170] For example, Li et al. prepared Ni electrodes with periodic pore structures based on 3D printing technology.^[171] As shown in Figure 12a, in the disordered structure of ordinary Ni foam, the bubble will encounter the force of different pore sizes and zigzag paths, which counteracts the effect of bubble buoyancy and thus affects the migration. In contrast, for 3D-printed electrodes with a periodic structure, the bubbles are able to pass through the electrodes and disassociate easily. As a result of this feature, the bubble migration in 3DPNi is significantly faster (Figure 12b). Surprisingly, C-Ni_{1-x}O/3DPNi delivered the large current densities of 1000 mA cm⁻² at an ultra-low overpotential of 245 mV in 1.0 M KOH. Similarly, Ho et al. developed a novel extrusion 3D printing technique to prepare NiMo-based electrodes with a significantly anisotropic structure (3DP NiMoAS).^[168] Compared to 3DP NiMoIS prepared with NiMoO₄·xH₂O nanoparticles/F127 prepared as printing inks, 3DP NiMoAS possesses a more rapid liquid transport channel, which facilitates the uptake and transfer of electrolytes (Figure 12c). In addition to this, benefiting from the capillary pressure generated by the long-range ordered structure of 3DP NiMoAS, the bubbles were induced to float up and out of the electrode and then pushed out of the structure along parallel channels (Figure 12d). Remarkably, the electrode has a very high stability, operating at 500 mA cm⁻² for 100 h in 1 M seawater without significant decay. 3D printing technology has great potential for the regular design and formation of electrode substrates, but its expensive price and lack of large-scale industrial deployment still limit its application in electrode substrate design.

In addition, using some unique materials as electrode substrates has been reported recently.^[172–175] For example, Guo et al. formed Ni-P-B/paper electrodes by chemically plating them on cheap and easily available substrates such as paper and sponge.^[173] The prepared paper electrodes possess good toughness, which facilitates their application in practical production. Furthermore, the Ni-P-B/paper electrode has a long lifespan, lasting for more than 240 h at 1000 mA cm⁻² and an overpotential of roughly 250 mV. In another work, Yi et al. prepared a MoNi₄/SSW electrode using waste SS wire from scrap tires as a substrate, which can produce a high current density of 1000 mA cm⁻² at $\eta = 161$ mV under industrial application conditions (5 M KOH, 343 K).^[172]

7. Summary and Outlook

Based on the laboratory R&D stage, developing alkaline HER electrocatalysts that maintain excellent stability at high current densities is critical for extending the development of the gradually stagnating alkaline water electrolysis hydrogen production industry. In this review, an overview of the HER reaction mechanisms is provided to elucidate the design challenges of HER catalysts eligible for industrial applications, and current design strategies for HER catalysts at the laboratory level are presented in terms of electronic structure regulation, active site modulation, and electrode design.

Although numerous excellent electrocatalysts have emerged from the scientific community, there is still a gap between the

lab and the industrial scale. Therefore, based on the current research achievements, we face many challenges to explore HER electrocatalysts for industrial applications. Finally, we will present some ideas and insights that would hopefully provide some contribution to the future development of this direction.

7.1. Scalable Green Synthesis Method for Large-Area Electrodes

Several excellent electrocatalysts maintain good stability at high current densities, but the main reason that usually limits their application is that the synthesis process is too complex and difficult to achieve large-scale production. Meanwhile, the size of electrodes operated in commercial alkaline electrolyzers is typically large, and the usual laboratory methods of solvent heat and electrodeposition are generally unable to achieve uniform catalyst growth over large areas. Therefore, the scalability of the synthesis method should be taken into account at the experimental design level in the R&D stage. Adaptation and development of existing preparation techniques and electrode materials is one way to solve the previously mentioned challenges. For example, the laboratory-stage excellent catalysts can be introduced into the electrodes using commercial thermal spray process. Meanwhile, secondary processing of commercial electrodes to upgrade the performance is also a promising approach. In addition, the development of new synthetic processes is another way to achieve large-scale production. Wet chemistry methods and 3D printing technologies all have the potential for easily scalable synthesis.

In addition to considering the scalability of the synthesis methods, economic considerations and environmental factors are necessary for the commercial application of catalysts. To achieve the economic benefits of electrodes, there is a need for further estimation of the cost consumption of the electrode preparation process and the pollution caused by the production.

7.2. Establishing Standardized Metrics for Performance Evaluation and Stability Prediction

Although HER catalysts for applications at high current densities have been well explored and addressed, the performance demonstrated in many papers may not be accurate. Most of the papers tend to correct the performance of HER catalysts with *iR* compensation, but the impedance of catalysts tends to decrease under high current test conditions, which will lead to a large error between the data obtained with *iR* compensation and the real properties.^[16,136] Moreover, there are often different percentages of *iR* compensation used in different papers, which also makes it more difficult to compare the performance of catalysts. The real-time impedance measurement is able to monitor the impedance of the electrodes in real-time and achieve automatic correction of the current values, which is a valuable way to circumvent the influence of impedance on catalyst performance assessment. Therefore, the application of real-time impedance measurement will be more convincing during catalyst performance testing. Meanwhile, HER catalysts are often required to have a long lifetime to meet commercial application standards, which also poses a significant obstacle for stability testing. Therefore, establishing a methodology for accelerated aging assessment in the laboratory

and industrial lifetime prediction may further facilitate the study of high-performance HER catalysts.

7.3. Rational Selection and Application of Electrode Substrates

As mentioned earlier, 3D porous metal materials are often used as electrode substrates in most of the papers to achieve a more excellent catalytic performance. Despite the milestones that can be achieved in the laboratory stage, porous electrodes may be mismatched with industrial electrolyzers in actual industrial use, which usually leads to excessive heat loss between the electrode and the electrolyzer, thus greatly limiting the further improvement of production efficiency. The selection and development of new dense electrode substrates during the R&D stage will enable a further increase in the production capacity of alkaline water electrolysis for hydrogen production. Currently, the most advanced AWE cell configuration is the zero-gap assembly. In this configuration, the irregular geometry of the 3D electrode is often not conducive to bubble removal, which severely limits the use of catalytic sites and the stability of the electrode.^[170] Therefore, the development of suitable electrode substrates and optimization of the electrolyzer structure configuration will be key to promoting further development of alkaline water electrolysis for hydrogen production.

7.4. Development of Advanced Characterization Techniques at High Current Densities

Further understanding of the catalytic mechanism and interfacial changes of high-performance catalysts under working conditions can help with the optimization and design of catalysts. Meanwhile, the catalytic mechanism of HER and catalyst deactivation is inseparable from the dynamic changes of electrocatalyst at the electrode–electrolyte interface, which is the basis for understanding the real structure–property relationship. Currently, numerous *in situ*/operational characterizations have been applied to electrocatalytic HER under conventional conditions, such as electrochemical-compatible *in situ* X-ray absorption spectroscopy, *in situ* Raman spectroscopy, and *in situ* atomic resolution electron transmission microscopy. However, the application of *in situ* characterization techniques is often limited or subjected to large error bars due to many factors, such as bubble perturbation at high current densities and rapid electron transfer and mass transfer efficiency. In general, there is still a long way to go in designing *in situ* characterization devices to overcome the problems resulting from high current densities and achieve accurate characterization.

7.5. Combining Accurate Theoretical Modeling with Experimental Development

The mechanism of HER under alkaline conditions is still heavily debated. Like the lack of *in situ* characterization techniques, most of the current models usually lack the consideration of the real dynamic evolution process in electrocatalysts under reaction conditions, so most of the theoretical calculations can only be used as a reference and cannot reflect the real reaction situation. For example, most of the theoretical calculations tend to build models that ignore the electrolyte and the local environmental changes under reaction conditions. Therefore, it is important to develop

a modeling approach and consider the realistic environment in conjunction with experimental findings. In addition, most catalyst designs are limited to “hearsay” in the literature or are subjected to extensive experimental trial and error. If theoretical big data-based screening can be used to help advance electrolytic catalyst exploration, this will provide greater opportunities and convenience for the whole field.

7.6. The Application and Design of Various Novel Devices for Alkaline Water Electrolysis

Alkaline water electrolysis has a long history of development and therefore has a mature device process. However, in the face of the expanding global demand for hydrogen and market competition, besides optimizing the electrode performance, the other focus of development is to upgrade the electrolyzer device to match the new electrocatalyst electrode, which can maximize the efficiency of hydrogen production. In addition to the aforementioned “zero-gap” electrolyzer, there is currently a significant interest in the design of anion-exchange membrane water electrolyzers (AEMWES) based on PEMWEs, which utilize an anion-exchange membrane instead of the physical diaphragm of an AWE and are used in conjunction with the PEMWE stack architecture. It combines the advantages of AWEs and PEMWEs to achieve a high rate of hydrogen production while using a non-noble metal catalyst. However, limited by the durability of the anion exchange membrane, the AEMWE is still in the early stages of development. In addition to AEMWES, Grimaud et al. have summarized other feasible water electrolyzer (WE) architectures and designs, such as membrane-less electrolyzers, controlled electron transfer using soluble media, and “battolyser” construction using auxiliary electrodes.^[22] Although these new electrolyzer devices are still far from being scaled up and deployed on a large scale, they are essential for the further expansion of AWE’s commercialization. Therefore, while designing excellent catalyst electrodes, it is worthwhile to think more deeply about developing better WE industrial components.

Acknowledgements

This work was financially supported by the Key Program of the National Natural Science Foundation of China (22239001), the International (Regional) Cooperation and Exchange Projects of the National Natural Science Foundation of China (51920105003), the Innovation Program of Shanghai Municipal Education Commission (E00014), the Science and Technology Commission of Shanghai Municipality (21DZ1207101, 22ZR1416400, 23YF1408500), the Shanghai Engineering Research Centre of Hierarchical Nanomaterials (18DZ2252400).

Conflict of Interest

The authors declare no conflict of interest.

Keywords

alkaline water electrolyzers, high current density, hydrogen evolution reactions, mass transfer, stability

Received: December 22, 2022
Revised: February 20, 2023
Published online:

- [1] P. Patrizio, Y. W. Pratama, N. M. Dowell, *Joule* **2020**, *4*, 1700.
 [2] S. Díaz, J. Settele, E. S. Brondízio, H. T. Ngo, J. Agard, A. Arneth, P. Balvanera, K. A. Brauman, S. H. M. Butchart, K. M. A. Chan, L. A. Garibaldi, K. Ichii, J. Liu, S. M. Subramanian, G. F. Midgley, P. Miloslavich, Z. Molnár, D. Obura, A. Pfaff, S. Polasky, A. Purvis, J. Razzaque, B. Reyers, R. R. Chowdhury, Y.-J. Shin, I. Visseren-Hamakers, K. J. Willis, C. N. Zayas, *Science* **2019**, *366*, eaax3100.
 [3] J. Meckling, C. Galeazzi, E. Shears, T. Xu, L. D. Anadon, *Nat. Energy* **2022**, *7*, 876.
 [4] G. Glenk, S. Reichelstein, *Nat. Energy* **2019**, *4*, 216.
 [5] IEA, *Cross-Cutting Technologies & Infrastructure*, IEA, Paris **2022**, <https://www.iea.org/reports/cross-cutting-technologies-infrastructure>.
 [6] D. Jang, J. Kim, D. Kim, W.-B. Han, S. Kang, *Energy Convers. Manage.* **2022**, 258.
 [7] S. Anwar, F. Khan, Y. Zhang, A. Djire, *Int. J. Hydrogen Energy* **2021**, *46*, 32284.
 [8] N. Mac Dowell, N. Sunny, N. Brandon, H. Herzog, A. Y. Ku, W. Maas, A. Ramirez, D. M. Reiner, G. N. Sant, N. Shah, *Joule* **2021**, *5*, 2524.
 [9] S. Marini, P. Salvi, P. Nelli, R. Pesenti, M. Villa, Y. Kiros, *Int. J. Hydrogen Energy* **2013**, *38*, 11484.
 [10] J. Mohammed-Ibrahim, X. Sun, *J. Energy Chem.* **2019**, *34*, 111.
 [11] A. R. Akbashev, *ACS Catal.* **2022**, *12*, 4296.
 [12] F. Pan, K. Huang, P. Liu, R. Li, C. Lian, H. Liu, J. Hu, *Small Struct.* **2022**, 2200248.
 [13] X. Zhang, M. Jin, F. Jia, J. Huang, A. Amini, S. Song, H. Yi, C. Cheng, *Energy Environ. Mater.* **2022**, Accepted Author Manuscript e12457. <https://doi.org/10.1002/eem.212457>.
 [14] Y. Zheng, Y. Jiao, M. Jaroniec, S. Z. Qiao, *Angew. Chem. Int. Ed.* **2015**, *54*, 52.
 [15] Y. Luo, Z. Zhang, M. Chhowalla, B. Liu, *Adv. Mater.* **2022**, *34*, 2108133.
 [16] H. Q. Fu, M. Zhou, P. F. Liu, P. Liu, H. Yin, K. Z. Sun, H. G. Yang, M. Al-Mamun, P. Hu, H. F. Wang, H. Zhao, *J. Am. Chem. Soc.* **2022**, *144*, 6028.
 [17] R. de Levie, *J. Electroanal. Chem.* **1999**, *476*, 92.
 [18] Z. Y. Yu, Y. Duan, X. Y. Feng, X. Yu, M. R. Gao, S. H. Yu, *Adv. Mater.* **2021**, *33*, 2007100.
 [19] S. A. Grigoriev, V. N. Fateev, D. G. Bessarabov, P. Millet, *Int. J. Hydrogen Energy* **2020**, *45*, 26036.
 [20] C. A. S. D. M. Santos, J. L. Figueiredo, *Quim. Nova* **2013**, *36*, 1176.
 [21] H. Xie, Z. Zhao, T. Liu, Y. Wu, C. Lan, W. Jiang, L. Zhu, Y. Wang, D. Yang, Z. Shao, *Nature* **2022**, *612*, 673.
 [22] M. F. Lagadec, A. Grimaud, *Nat. Mater.* **2020**, *19*, 1140.
 [23] Clean Hydrogen JU, *Multi - Annual Work Plan 2014-2020 2018*, <https://wayback.archive-it.org/12090/20220602161820/> https://www.clean-hydrogen.europa.eu/knowledge-management/key-performance-indicators-kpis_en.
 [24] M. M. Roubelakis, D. K. Bediako, D. K. Dogutan, D. G. Nocera, *Energy Environ. Sci.* **2012**, *5*, 7737.
 [25] N. Elgrishi, B. D. McCarthy, E. S. Rountree, J. L. Dempsey, *ACS Catal.* **2016**, *6*, 3644.
 [26] J. Chen, C. Chen, M. Qin, B. Li, B. Lin, Q. Mao, H. Yang, B. Liu, Y. Wang, *Nat. Commun.* **2022**, *13*, 5382.
 [27] H. Prats, K. Chan, *Phys. Chem. Chem. Phys.* **2021**, *23*, 27150.
 [28] E. Skúlason, V. Tripkovic, M. E. Björketun, S. Gudmundsdóttir, G. Karlberg, J. Rossmeisl, T. Bligaard, H. Jónsson, J. K. Nørskov, *J. Phys. Chem. C* **2010**, *114*, 18182.
 [29] Y. Liu, Q. Feng, W. Liu, Q. Li, Y. Wang, B. Liu, L. Zheng, W. Wang, L. Huang, L. Chen, X. Xiong, Y. Lei, *Nano Energy* **2021**, *81*, 105641.
 [30] C. Das, N. Sinha, P. Roy, *Small* **2022**, *18*, 2202033.
 [31] W. Sheng, Z. Zhuang, M. Gao, J. Zheng, J. G. Chen, Y. Yan, *Nat. Commun.* **2015**, *6*, 5848.
 [32] J. Zheng, W. Sheng, Z. Zhuang, B. Xu, Y. Yan, *Adv. Sci.* **2016**, *2*, 1501602.
 [33] R. Subbaraman, D. Tripkovic, K. C. Chang, D. Strmcnik, A. P. Paulikas, P. Hirunsit, M. Chan, J. Greeley, V. Stamenkovic, N. M. Markovic, *Nat. Mater.* **2012**, *11*, 550.
 [34] I. T. McCrum, M. T. M. Koper, *Nat. Energy* **2020**, *5*, 891.
 [35] R. Subbaraman, D. Tripkovic, D. Strmcnik, K.-C. Chang, M. Uchimura, A. P. Paulikas, V. Stamenkovic, N. M. Markovic, *Science* **2011**, *334*, 1256.
 [36] N. Ramaswamy, S. Ghoshal, M. K. Bates, Q. Jia, J. Li, S. Mukerjee, *Nano Energy* **2017**, *41*, 765.
 [37] F. Liu, C. Shi, X. Guo, Z. He, L. Pan, Z. F. Huang, X. Zhang, J. J. Zou, *Adv. Sci.* **2022**, *9*, 2200307.
 [38] H. Yu, X. Yu, Y. Chen, S. Zhang, P. Gao, C. Li, *Nanoscale* **2015**, *7*, 8731.
 [39] B. Zhou, R. Gao, J. J. Zou, H. Yang, *Small* **2022**, *18*, 2202336.
 [40] D. Strmcnik, M. Uchimura, C. Wang, R. Subbaraman, N. Danilovic, D. van der Vliet, A. P. Paulikas, V. R. Stamenkovic, N. M. Markovic, *Nat. Chem.* **2013**, *5*, 300.
 [41] F. Sun, Q. Tang, D. Jiang, *ACS Catal.* **2022**, *12*, 8404.
 [42] D. Voiry, R. Fullon, J. Yang, E. S. C. de Carvalho Castro, R. Kappera, I. Bozkurt, D. Kaplan, M. J. Lagos, P. E. Batson, G. Gupta, A. D. Mohite, L. Dong, D. Er, V. B. Shenoy, T. Asefa, M. Chhowalla, *Nat. Mater.* **2016**, *15*, 1003.
 [43] R. Ye, P. del Angel-Vicente, Y. Liu, M. J. Arellano-Jimenez, Z. Peng, T. Wang, Y. Li, B. I. Yakobson, S. H. Wei, M. J. Yacaman, J. M. Tour, *Adv. Mater.* **2016**, *28*, 1427.
 [44] M. Yu, Z. Wang, J. Liu, F. Sun, P. Yang, J. Qiu, *Nano Energy* **2019**, *63*, 103880.
 [45] M. Wang, K. Jian, Z. Lv, D. Li, G. Fan, R. Zhang, J. Dang, *J Mater Sci Technol* **2021**, *79*, 29.
 [46] Z. Lv, W. Ma, M. Wang, J. Dang, K. Jian, D. Liu, D. Huang, *Adv. Funct. Mater.* **2021**, *31*, 2102576.
 [47] J. Bao, X. Zhang, B. Fan, J. Zhang, M. Zhou, W. Yang, X. Hu, H. Wang, B. Pan, Y. Xie, *Angew. Chem. Int. Ed.* **2015**, *54*, 7399.
 [48] Y. Li, H. Zhang, T. Xu, Z. Lu, X. Wu, P. Wan, X. Sun, L. Jiang, *Adv. Funct. Mater.* **2015**, *25*, 1737.
 [49] Z. Lu, Y. Li, X. Lei, J. Liu, X. Sun, *Mater. Horiz.* **2015**, *2*, 294.
 [50] Y. Luo, L. Tang, U. Khan, Q. Yu, H. M. Cheng, X. Zou, B. Liu, *Nat. Commun.* **2019**, *10*, 269.
 [51] H. Li, L. Li, Y. Li, *Nanotechnol. Rev.* **2013**, *2*, 515.
 [52] A. J. Martín, S. Mitchell, C. Mondelli, S. Jaydev, J. Pérez-Ramírez, *Nat. Catal.* **2022**, *5*, 854.
 [53] H. Jin, B. Ruqia, Y. Park, H. J. Kim, H. S. Oh, S. I. Choi, K. Lee, *Adv. Energy Mater.* **2021**, *11*, 2003188.
 [54] P. van der Linde, P. Peñas-López, Á. Moreno Soto, D. van der Meer, D. Lohse, H. Gardeniers, D. Fernández Rivas, *Energy Environ. Sci.* **2018**, *11*, 3452.
 [55] J. Zhang, F. Dong, C. Wang, J. Wang, L. Jiang, C. Yu, *ACS Appl. Mater. Interfaces* **2021**, *13*, 32435.
 [56] J. Kim, A. Park, J. Kim, S. J. Kwak, J. Y. Lee, D. Lee, S. Kim, B. K. Choi, S. Kim, J. Kwag, Y. Kim, S. Jeon, W. C. Lee, T. Hyeon, C. H. Lee, W. B. Lee, J. Park, *Adv. Mater.* **2022**, *34*, 2206066.
 [57] A. Angulo, P. van der Linde, H. Gardeniers, M. Modestino, D. Fernández Rivas, *Joule* **2020**, *4*, 555.
 [58] W. Yang, L. Sun, J. Tang, Z. Mo, H. Liu, M. Du, J. Bao, *Ind. Eng. Chem. Res.* **2022**, *61*, 8323.
 [59] J. Dukovic, C. W. Tobias, *J. Electrochem. Soc.* **1987**, *134*, 331.
 [60] Y. Chen, J. Chen, K. Bai, Z. Xiao, S. Fan, *J. Power Sources* **2023**, *561*, 232733.

- [61] L. Li, P. C. M. Laan, X. Yan, X. Cao, M. J. Mekkerink, K. Zhao, L. Ke, X. Jiang, X. Wu, L. Li, L. Xue, Z. Wang, G. Rothenberg, N. Yan, *Adv. Sci.* **2022**, *10*, 2206180.
- [62] J. W. Haverkort, H. Rajaei, *J. Power Sources* **2021**, *497*, 229864.
- [63] K. Zeng, D. Zhang, *Prog. Energy Combust. Sci.* **2010**, *36*, 307.
- [64] X. Y. Wong, Y. Zhuo, Y. Shen, *Ind. Eng. Chem. Res.* **2021**, *60*, 12429.
- [65] M. T. de Groot, A. W. Vreman, *Electrochim. Acta* **2021**, *369*, 137684.
- [66] A. Manabe, M. Kashiwase, T. Hashimoto, T. Hayashida, A. Kato, K. Hirao, I. Shimomura, I. Nagashima, *Electrochim. Acta* **2013**, *100*, 249.
- [67] Q. Song, Z. Xue, C. Liu, X. Qiao, L. Liu, C. Huang, K. Liu, X. Li, Z. Lu, T. Wang, *J. Am. Chem. Soc.* **2020**, *142*, 1857.
- [68] X. Wu, J. Qiu, Z. Wang, *Small Struct.* **2022**, 2200268.
- [69] X. Wang, W. Ma, C. Ding, Z. Xu, H. Wang, X. Zong, C. Li, *ACS Catal.* **2018**, *8*, 9926.
- [70] Y. Shi, Y. Zhou, D. R. Yang, W. X. Xu, C. Wang, F. B. Wang, J. J. Xu, X. H. Xia, H. Y. Chen, *J. Am. Chem. Soc.* **2017**, *139*, 15479.
- [71] H. Sun, Y. Min, W. Yang, Y. Lian, L. Lin, K. Feng, Z. Deng, M. Chen, J. Zhong, L. Xu, Y. Peng, *ACS Catal.* **2019**, *9*, 8882.
- [72] L. Hui, Y. Xue, D. Jia, H. Yu, C. Zhang, Y. Li, *Adv. Energy Mater.* **2018**, *8*, 1800175.
- [73] J. Jian, L. Yuan, H. Qi, X. Sun, L. Zhang, H. Li, H. Yuan, S. Feng, *ACS Appl. Mater. Interfaces* **2018**, *10*, 40568.
- [74] Y. Rao, S. Wang, R. Zhang, S. Jiang, S. Chen, Y. Yu, S. Bao, M. Xu, Q. Yue, H. Xin, Y. Kang, *ACS Appl. Mater. Interfaces* **2020**, *12*, 37092.
- [75] X. Y. Zhang, Y. R. Zhu, Y. Chen, S. Y. Dou, X. Y. Chen, B. Dong, B. Y. Guo, D. P. Liu, C. G. Liu, Y. M. Chai, *Chem. Eng. J.* **2020**, *399*, 125831.
- [76] W. He, L. Han, Q. Hao, X. Zheng, Y. Li, J. Zhang, C. Liu, H. Liu, H. L. Xin, *ACS Energy Lett.* **2019**, *4*, 2905.
- [77] S. H. Ahn, A. Manthiram, *Small* **2020**, *16*, 2002511.
- [78] W. Yu, H. Huang, Y. Qin, D. Zhang, Y. Zhang, K. Liu, Y. Zhang, J. Lai, L. Wang, *Adv. Energy Mater.* **2022**, *12*, 2200110.
- [79] Y. Chen, J. Yu, J. Jia, F. Liu, Y. Zhang, G. Xiong, R. Zhang, R. Yang, D. Sun, H. Liu, W. Zhou, *Appl. Catal. B* **2020**, *272*, 118956.
- [80] C. Huang, L. Yu, W. Zhang, Q. Xiao, J. Zhou, Y. Zhang, P. An, J. Zhang, Y. Yu, *Appl. Catal. B* **2020**, *276*, 119137.
- [81] H. Yang, Z. Chen, P. Guo, B. Fei, R. Wu, *Appl. Catal. B* **2020**, *261*, 118240.
- [82] J. X. Wei, M. Z. Cao, K. Xiao, X. P. Guo, S. Y. Ye, Z. Q. Liu, *Small Struct.* **2021**, *2*, 2100047.
- [83] Y. Qiu, S. Liu, C. Wei, J. Fan, H. Yao, L. Dai, G. Wang, H. Li, B. Su, X. Guo, *Chem. Eng. J.* **2022**, *427*, 131309.
- [84] Z. Luo, R. Miao, T. D. Huan, I. M. Mosa, A. S. Poyraz, W. Zhong, J. E. Cloud, D. A. Kriz, S. Thanneeru, J. He, Y. Zhang, R. Ramprasad, S. L. Suib, *Adv. Energy Mater.* **2016**, *6*, 1600528.
- [85] Y. Y. Chen, Y. Zhang, X. Zhang, T. Tang, H. Luo, S. Niu, Z. H. Dai, L. J. Wan, J. S. Hu, *Adv Mater* **2017**, *29*, 1703311.
- [86] Y. Zhai, X. Ren, J. Yan, S. Liu, *Small Struct.* **2020**, *2*, 2000096.
- [87] X. Shan, J. Liu, H. Mu, Y. Xiao, B. Mei, W. Liu, G. Lin, Z. Jiang, L. Wen, L. Jiang, *Angew. Chem. Int. Ed.* **2020**, *59*, 1659.
- [88] P. Ji, R. Yu, P. Wang, X. Pan, H. Jin, D. Zheng, D. Chen, J. Zhu, Z. Pu, J. Wu, S. Mu, *Adv. Sci.* **2022**, *9*, 2103567.
- [89] P. Zhai, Y. Zhang, Y. Wu, J. Gao, B. Zhang, S. Cao, Y. Zhang, Z. Li, L. Sun, J. Hou, *Nat. Commun.* **2020**, *11*, 5462.
- [90] S. Xue, Z. Liu, C. Ma, H.-M. Cheng, W. Ren, *Sci. Bull.* **2020**, *65*, 123.
- [91] B. Ren, D. Li, Q. Jin, H. Cui, C. Wang, *J. Mater. Chem. A* **2017**, *5*, 24453.
- [92] L. Wang, Y. Hao, L. Deng, F. Hu, S. Zhao, L. Li, S. Peng, *Nat. Commun.* **2022**, *13*, 5785.
- [93] F. Yu, H. Zhou, Y. Huang, J. Sun, F. Qin, J. Bao, W. A. Goddard3rd3rd, S. Chen, Z. Ren, *Nat. Commun.* **2018**, *9*, 2551.
- [94] M. Jin, X. Zhang, R. Shi, Q. Lian, S. Niu, O. Peng, Q. Wang, C. Cheng, *Appl. Catal. B* **2021**, *296*, 120350.
- [95] C. Li, W. Hong, Q. Cai, C. Jian, *ACS Appl. Mater. Interfaces* **2022**, *14*, 30683.
- [96] M. Zhou, Q. Weng, Z. I. Popov, Y. Yang, L. Y. Antipina, P. B. Sorokin, X. Wang, Y. Bando, D. Golberg, *ACS Nano* **2018**, *12*, 4148.
- [97] Q. Liu, Q. Fang, W. Chu, Y. Wan, X. Li, W. Xu, M. Habib, S. Tao, Y. Zhou, D. Liu, T. Xiang, A. Khalil, X. Wu, M. Chhowalla, P. M. Ajayan, L. Song, *Chem. Mater.* **2017**, *29*, 4738.
- [98] Y. Li, X. Wu, H. Zhang, J. Zhang, *ACS Appl. Energy Mater.* **2018**, *1*, 3377.
- [99] Y. Qiu, Z. Liu, X. Zhang, A. Sun, J. Liu, *Appl. Surf. Sci.* **2022**, *598*, 153690.
- [100] B. You, Y. Zhang, Y. Jiao, K. Davey, S. Z. Qiao, *Angew. Chem. Int. Ed.* **2019**, *58*, 11796.
- [101] S. Ma, X. Qu, J. Huang, C. Zhang, G. Chen, W. Chen, T. Li, T. Shao, K. Zheng, J. Tian, C. Li, K. Ostrikov, *Nano Energy* **2022**, *95*, 106989.
- [102] H. Yu, X. Yang, X. Xiao, M. Chen, Q. Zhang, L. Huang, J. Wu, T. Li, S. Chen, L. Song, L. Gu, B. Y. Xia, G. Feng, J. Li, J. Zhou, *Adv. Mater.* **2018**, *30*, 1805655.
- [103] L. Yu, Q. Zhu, S. Song, B. McElhenney, D. Wang, C. Wu, Z. Qin, J. Bao, Y. Yu, S. Chen, Z. Ren, *Nat. Commun.* **2019**, *10*, 5106.
- [104] F. Lin, Z. Dong, Y. Yao, L. Yang, F. Fang, L. Jiao, *Adv. Energy Mater.* **2020**, *10*, 2002176.
- [105] H. Sun, C. Tian, G. Fan, J. Qi, Z. Liu, Z. Yan, F. Cheng, J. Chen, C. P. Li, M. Du, *Adv. Funct. Mater.* **2020**, *30*, 1910596.
- [106] J. N. Tiwari, A. M. Harzandi, M. Ha, S. Sultan, C. W. Myung, H. J. Park, D. Y. Kim, P. Thangavel, A. N. Singh, P. Sharma, S. S. Chandrasekaran, F. Salehnia, J. W. Jang, H. S. Shin, Z. Lee, K. S. Kim, *Adv. Energy Mater.* **2019**, *9*, 1900931.
- [107] J. Xu, T. Liu, J. Li, B. Li, Y. Liu, B. Zhang, D. Xiong, I. Amorim, W. Li, L. Liu, *Energy Environ. Sci.* **2018**, *11*, 1819.
- [108] G. Chen, T. Wang, J. Zhang, P. Liu, H. Sun, X. Zhuang, M. Chen, X. Feng, *Adv. Mater.* **2018**, *30*, 1706279.
- [109] G. Zhang, B. Wang, L. Li, S. Yang, J. Liu, S. Yang, *J. Mater. Chem. A* **2020**, *8*, 18945.
- [110] L.-N. Zhang, Z.-L. Lang, Y.-H. Wang, H.-Q. Tan, H.-Y. Zang, Z.-H. Kang, Y.-G. Li, *Energy Environ. Sci.* **2019**, *12*, 2569.
- [111] Y. Zhang, K. E. Arpino, Q. Yang, N. Kikugawa, D. A. Sokolov, C. W. Hicks, J. Liu, C. Felser, G. Li, *Nat. Commun.* **2022**, *13*, 7784.
- [112] G. Zhao, Y. Jiang, S.-X. Dou, W. Sun, H. Pan, *Sci. Bull.* **2021**, *66*, 85.
- [113] Y. Yao, Y. Zhu, C. Pan, C. Wang, S. Hu, W. Xiao, X. Chi, Y. Fang, J. Yang, H. Deng, S. Xiao, J. Li, Z. Luo, Y. Guo, *J. Am. Chem. Soc.* **2021**, *143*, 8720.
- [114] X. Wang, Y. Zheng, W. Sheng, Z. J. Xu, M. Jaroniec, S.-Z. Qiao, *Mater. Today* **2020**, *36*, 125.
- [115] C. Yang, W. Zhong, K. Shen, Q. Zhang, R. Zhao, H. Xiang, J. Wu, X. Li, N. Yang, *Adv. Energy Mater.* **2022**, *12*, 2200077.
- [116] H. Wu, L. Kong, Y. Ji, J. Yan, Y. Ding, Y. Li, S. T. Lee, S. Liu, *Adv. Mater. Interfaces* **2019**, *6*, 1900308.
- [117] J. Zhang, X. Shang, H. Ren, J. Chi, H. Fu, B. Dong, C. Liu, Y. Chai, *Adv. Mater.* **2019**, *31*, 1905107.
- [118] H. Sun, X. Xu, Z. Yan, X. Chen, L. Jiao, F. Cheng, J. Chen, *J. Mater. Chem. A* **2018**, *6*, 22062.
- [119] H. Zhang, X. Wu, C. Chen, C. Lv, H. Liu, Y. Lv, J. Guo, J. Li, D. Jia, F. Tong, *Chem. Eng. J.* **2021**, *417*, 128069.
- [120] T. Wu, E. Song, S. Zhang, M. Luo, C. Zhao, W. Zhao, J. Liu, F. Huang, *Adv. Mater.* **2022**, *34*, 2108505.
- [121] Y. Zhou, R. Li, L. Dong, S. Yin, B. Chu, Z. Chen, J. Wang, B. Li, M. Fan, *ACS Appl. Mater. Interfaces* **2022**, *14*, 18816.
- [122] J. Huang, C. Jian, Q. Cai, W. Hong, W. Liu, *J. Mater. Chem. A* **2022**, *10*, 10990.
- [123] Q. Che, X. Zhou, Q. Liu, Y. Tan, Q. Li, *J. Mater. Chem. A* **2021**, *9*, 5833.

- [124] X. Mu, X. Gu, S. Dai, J. Chen, Y. Cui, Q. Chen, M. Yu, C. Chen, S. Liu, S. Mu, *Energy Environ. Sci.* **2022**, *15*, 4048.
- [125] T. Luo, J. Huang, Y. Hu, C. Yuan, J. Chen, L. Cao, K. Kajiyoshi, Y. Liu, Y. Zhao, Z. Li, Y. Feng, *Adv. Funct. Mater.* **2023**, 2213058.
- [126] J. Chen, Y. Wang, G. Qian, T. Yu, Z. Wang, L. Luo, F. Shen, S. Yin, *Chem. Eng. J.* **2021**, *421*, 129892.
- [127] Y. Wu, G.-D. Li, Y. Liu, L. Yang, X. Lian, T. Asefa, X. Zou, *Adv. Funct. Mater.* **2016**, *26*, 4839.
- [128] J. Tian, Z. Xing, Q. Chu, Q. Liu, A. M. Asiri, A. H. Qusti, A. O. Al-Youbi, X. Sun, *CrystEngComm* **2013**, *15*, 8300.
- [129] J. Zhang, T. Wang, P. Liu, Z. Liao, S. Liu, X. Zhuang, M. Chen, E. Zschech, X. Feng, *Nat. Commun.* **2017**, *8*, 15437.
- [130] D. Zhang, F. Wang, W. Zhao, M. Cui, X. Fan, R. Liang, Q. Ou, S. Zhang, *Adv. Sci.* **2022**, *9*, 2202445.
- [131] Y. Sun, Y. Zang, W. Tian, X. Yu, J. Qi, L. Chen, X. Liu, H. Qiu, *Energy Environ. Sci.* **2022**, *15*, 1201.
- [132] X. Tong, Y. Li, Q. Ruan, N. Pang, Y. Zhou, D. Wu, D. Xiong, S. Xu, L. Wang, P. K. Chu, *Adv. Sci.* **2022**, *9*, 2104774.
- [133] Y. Yan, J. Lin, T. Xu, B. Liu, K. Huang, L. Qiao, S. Liu, J. Cao, S. C. Jun, Y. Yamauchi, J. Qi, *Adv. Energy Mater.* **2022**, *12*, 2200434.
- [134] Q. Han, *Int. J. Hydrogen Energy* **2004**, *29*, 243.
- [135] Q. Han, X. Li, J. Chen, K. Liu, X. Dong, X. Wei, *J. Alloys Compd.* **2005**, *400*, 265.
- [136] X. Chen, X. Zhao, Y. Wang, S. Wang, Y. Shang, J. Xu, F. Guo, Y. Zhang, *ChemCatChem* **2021**, *13*, 3619.
- [137] X. Liu, Y. Yao, H. Zhang, L. Pan, C. Shi, X. Zhang, Z.-F. Huang, J.-J. Zou, *ACS Sustainable Chem. Eng.* **2020**, *8*, 17828.
- [138] C. Yu, F. Xu, L. Luo, H. S. Abbo, S. J. J. Titinchi, P. K. Shen, P. Tsakaratas, S. Yin, *Electrochim. Acta* **2019**, *317*, 191.
- [139] S. Parvin, A. Kumar, A. Ghosh, S. Bhattacharyya, *Chem. Sci.* **2020**, *11*, 3893.
- [140] Y. Li, B. Wei, Z. Yu, O. Bondarchuk, A. Araujo, I. Amorim, N. Zhang, J. Xu, I. C. Neves, L. Liu, *ACS Sustainable Chem. Eng.* **2020**, *8*, 10193.
- [141] W. Hao, R. Wu, R. Zhang, Y. Ha, Z. Chen, L. Wang, Y. Yang, X. Ma, D. Sun, F. Fang, Y. Guo, *Adv. Energy Mater.* **2018**, *8*, 1801372.
- [142] R. Zhang, H. Liu, C. Wang, L. Wang, Y. Yang, Y. Guo, *ChemCatChem* **2020**, *12*, 3068.
- [143] J. Zhang, L. Chen, B. Lu, Y. Guo, *ChemSusChem* **2022**, *15*, e202200937.
- [144] L. Wang, T. Weissbach, R. Reissner, A. Ansar, A. S. Gago, S. Holdcroft, K. A. Friedrich, *ACS Appl. Energy Mater.* **2019**, *2*, 7903.
- [145] D. Chade, L. Berlouis, D. Infield, A. Cruden, P. T. Nielsen, T. Mathiesen, *Int. J. Hydrogen Energy* **2013**, *38*, 14380.
- [146] W. J. Kang, Y. Feng, Z. Li, W. Q. Yang, C. Q. Cheng, Z. Z. Shi, P. F. Yin, G. R. Shen, J. Yang, C. K. Dong, H. Liu, F. X. Ye, X. W. Du, *Adv. Funct. Mater.* **2022**, *32*, 2112367.
- [147] H. Liu, R. Xie, Y. Luo, Z. Cui, Q. Yu, Z. Gao, Z. Zhang, F. Yang, X. Kang, S. Ge, S. Li, X. Gao, G. Chai, L. Liu, B. Liu, *Nat. Commun.* **2022**, *13*, 6382.
- [148] I. K. Mishra, H. Zhou, J. Sun, F. Qin, K. Dahal, J. Bao, S. Chen, Z. Ren, *Energy Environ. Sci.* **2018**, *11*, 2246.
- [149] T. Wang, Z. Hong, F. Sun, B. Wang, C. Jian, W. Liu, *RSC Adv.* **2022**, *12*, 27225.
- [150] S. Zhang, W. Wang, F. Hu, Y. Mi, S. Wang, Y. Liu, X. Ai, J. Fang, H. Li, T. Zhai, *Nanomicro Lett.* **2020**, *12*, 140.
- [151] K. Z. Sun, C. F. Wen, X. Qu, P. F. Liu, H. G. Yang, *Small Methods* **2022**, *6*, 2200484.
- [152] L. Yu, I. K. Mishra, Y. Xie, H. Zhou, J. Sun, J. Zhou, Y. Ni, D. Luo, F. Yu, Y. Yu, S. Chen, Z. Ren, *Nano Energy* **2018**, *53*, 492.
- [153] D. Gao, J. Ren, H. Wang, X. Wang, Y. Liu, R. Wang, *J. Power Sources* **2021**, *516*, 230635.
- [154] M. Fang, W. Gao, G. Dong, Z. Xia, S. Yip, Y. Qin, Y. Qu, J. C. Ho, *Nano Energy* **2016**, *27*, 247.
- [155] J. Pan, S. Yu, Z. Jing, Q. Zhou, Y. Dong, X. Lou, F. Xia, *Small Struct.* **2021**, *2*, 2100076.
- [156] T. Kou, S. Wang, Y. Li, *ACS Mater. Lett.* **2021**, *3*, 224.
- [157] W. Xu, Z. Lu, X. Sun, L. Jiang, X. Duan, *Acc. Chem. Res.* **2018**, *51*, 1590.
- [158] J. E. George, S. Chidangil, S. D. George, *Adv. Mater. Interfaces* **2017**, *4*, 1601088.
- [159] X. Yu, Z. Y. Yu, X. L. Zhang, Y. R. Zheng, Y. Duan, Q. Gao, R. Wu, B. Sun, M. R. Gao, G. Wang, S. H. Yu, *J. Am. Chem. Soc.* **2019**, *141*, 7537.
- [160] H. Li, S. Chen, Y. Zhang, Q. Zhang, X. Jia, Q. Zhang, L. Gu, X. Sun, L. Song, X. Wang, *Nat. Commun.* **2018**, *9*, 2452.
- [161] F. Yang, Y. Luo, Q. Yu, Z. Zhang, S. Zhang, Z. Liu, W. Ren, H. M. Cheng, J. Li, B. Liu, *Adv. Funct. Mater.* **2021**, *31*, 2010367.
- [162] Y. Luo, Z. Zhang, F. Yang, J. Li, Z. Liu, W. Ren, S. Zhang, B. Liu, *Energy Environ. Sci.* **2021**, *14*, 4610.
- [163] J. Jian, W. Chen, D. Zeng, L. Chang, R. Zhang, M. Jiang, G. Yu, X. Huang, H. Yuan, S. Feng, *J. Mater. Chem. A* **2021**, *9*, 7586.
- [164] M. Bae, Y. Kang, D. W. Lee, D. Jeon, J. Ryu, *Adv. Energy Mater.* **2022**, *12*, 2201452.
- [165] L. Zhang, J. Huang, Q. Zheng, A. Li, X. Li, J. Li, M. Shao, H. Chen, Z. Wei, Z. Deng, C. Li, *Chem. Commun.* **2021**, *57*, 6173.
- [166] I. Sullivan, H. Zhang, C. Zhu, M. Wood, A. J. Nelson, S. E. Baker, C. M. Spadaccini, T. Van Buuren, M. Lin, E. B. Duoss, S. Liang, C. Xiang, *ACS Appl. Mater. Interfaces* **2021**, *13*, 20260.
- [167] R. A. Marquez, K. Kawashima, Y. J. Son, R. Rose, L. A. Smith, N. Miller, O. A. Carrasco Jaim, H. Celio, C. B. Mullins, *ACS Appl. Mater. Interfaces* **2022**, *14*, 42153.
- [168] X. Bu, Z. Mao, Y. Bu, Q. Quan, Y. Meng, Z. Lai, D. Chen, P. Xie, H. Li, C. Liu, X. Wang, S. Yip, J. Lu, J. C. Ho, *Appl. Catal. B* **2023**, *320*, 121995.
- [169] X. Xue, D. Lin, Y. Li, *Small Struct.* **2022**, *3*, 2200159.
- [170] F. Rocha, R. Delmelle, C. Georgiadis, J. Proost, *Adv. Energy Mater.* **2023**, *13*, 2203087.
- [171] T. Kou, S. Wang, R. Shi, T. Zhang, S. Chiavoloni, J. Q. Lu, W. Chen, M. A. Worsley, B. C. Wood, S. E. Baker, E. B. Duoss, R. Wu, C. Zhu, Y. Li, *Adv. Energy Mater.* **2020**, *10*, 2002955.
- [172] V. R. Jothi, K. Karuppasamy, T. Maiyalagan, H. Rajan, C. Y. Jung, S. C. Yi, *Adv. Energy Mater.* **2020**, *10*, 1904020.
- [173] W. Hao, R. Wu, H. Huang, X. Ou, L. Wang, D. Sun, X. Ma, Y. Guo, *Energy Environ. Sci.* **2020**, *13*, 102.
- [174] B. Hui, K. Zhang, Y. Xia, C. Zhou, *Electrochim. Acta* **2020**, *330*, 135274.
- [175] P. Zhou, P. Niu, J. Liu, N. Zhang, H. Bai, M. Chen, J. Feng, D. Liu, L. Wang, S. Chen, C. T. Kwok, Y. Tang, R. Li, S. Wang, H. Pan, *Adv. Funct. Mater.* **2022**, *32*, 2202068.



Hao Guan Xu received his B.S. degree from the East China University of Science and Technology in 2021. He is currently a Ph.D. candidate under the supervision of Prof. Hua Gui Yang in School of Materials Science and Engineering at the East China University of Science and Technology. His current research interests are focused on the design and fabrication of advanced catalysts for alkaline water electrolysis.



Peng Fei Liu received his B.S. and Ph.D. degrees from the East China University of Science and Technology (ECUST) in 2013 and 2018, respectively, and then worked in Prof. Hua Gui Yang's group as a Postdoctoral Research Fellow and an Associate Research Fellow. From 2023 to present, he worked as an Associate Professor at ECUST. His current research interests are focused on the design and synthesis of inorganic functional materials with well-defined structures for electrocatalysis.



Hua Gui Yang received his Ph.D. degree from the National University of Singapore in 2005. He joined the University of Queensland in 2007 as a Postdoctoral Research Fellow. After finishing his postdoctoral training, he came back to China and took a professor position at the East China University of Science and Technology at the end of 2008. His main research interests are focused on the rational design and fabrication of functional materials for solar fuels.